A&A 603, A81 (2017)
DOI: 10.1051/0004-6361/201629020

Astronomy & Astrophysics

Gaia-ESO Survey: Global properties of clusters Trumpler 14 and 16 in the Carina nebula[⋆,⋆⋆]

F. Damiani[1], A. Klutsch[2], R. D. Jeffries[3], S. Randich[4], L. Prisinzano[1], J. Maíz Apellániz[5], G. Micela[1], V. Kalari[6,7], A. Frasca[2], T. Zwitter[8], R. Bonito[1,9], G. Gilmore[10], E. Flaccomio[1], P. Francois[11], S. Koposov[10,12], A. C. Lanzafame[13], G. G. Sacco[4], A. Bayo[14], G. Carraro[15], A. R. Casey[10], E. J. Alfaro[16], M. T. Costado[16], P. Donati[17], E. Franciosini[4], A. Hourihane[10], P. Jofré[10,18], C. Lardo[19], J. Lewis[10], L. Magrini[4], L. Monaco[20], L. Morbidelli[4], C. C. Worley[10], J. S. Vink[6], and S. Zaggia[21]

[1] INAF–Osservatorio Astronomico di Palermo G. S. Vaiana, Piazza del Parlamento 1, 90134 Palermo, Italy
e-mail: damiani@astropa.inaf.it
[2] INAF–Osservatorio Astrofisico di Catania, via S. Sofia 78, 95123 Catania, Italy
[3] Astrophysics Group, Keele University, Keele, Staffordshire ST5 5BG, UK
[4] INAF–Osservatorio Astrofisico di Arcetri, Largo E. Fermi 5, 50125 Firenze, Italy
[5] Centro de Astrobiología (CSIC-INTA), ESAC campus, Camino bajo del castillo s/n, 28 692 Villanueva de la Cañada, Madrid, Spain
[6] Armagh Observatory, College Hill, Armagh BT61 9DG, UK
[7] School of Mathematics & Physics, Queen's University Belfast, Belfast BT61 7NN, UK
[8] Faculty of Mathematics and Physics, University of Ljubljana, Jadranska 19, 1000 Ljubljana, Slovenia
[9] Dipartimento di Fisica e Chimica, Università di Palermo, Piazza del Parlamento 1, 90134 Palermo, Italy
[10] Institute of Astronomy, University of Cambridge, Madingley Road, Cambridge CB3 0HA, UK
[11] GEPI, Observatoire de Paris, CNRS, Université Paris Diderot, 5 place Jules Janssen, 92190 Meudon, France
[12] Moscow MV Lomonosov State University, Sternberg Astronomical Institute, Moscow 119992, Russia
[13] Dipartimento di Fisica e Astronomia, Sezione Astrofisica, Università di Catania, via S. Sofia 78, 95123 Catania, Italy
[14] Instituto de Física y Astronomiía, Universidad de Valparaiíso, Chile
[15] European Southern Observatory, Alonso de Cordova 3107 Vitacura, Santiago de Chile, Chile
[16] Instituto de Astrofísica de Andalucía-CSIC, Apdo. 3004, 18080 Granada, Spain
[17] INAF–Osservatorio Astronomico di Bologna, via Ranzani 1, 40127 Bologna, Italy
[18] Núcleo de Astronomía, Facultad de Ingeniería, Universidad Diego Portales, Av. Ejercito 441, Santiago, Chile
[19] Astrophysics Research Institute, Liverpool John Moores University, 146 Brownlow Hill, Liverpool L3 5RF, UK
[20] Departamento de Ciencias Fisicas, Universidad Andres Bello, Republica 220, Santiago, Chile
[21] INAF–Osservatorio Astronomico di Padova, Vicolo dell'Osservatorio 5, 35122 Padova, Italy

Received 27 May 2016 / Accepted 14 February 2017

ABSTRACT

Aims. We present the first extensive spectroscopic study of the global population in star clusters Trumpler 16, Trumpler 14, and Collinder 232 in the Carina nebula, using data from the *Gaia*-ESO Survey, down to solar-mass stars.
Methods. In addition to the standard homogeneous survey data reduction, a special processing was applied here because of the bright nebulosity surrounding Carina stars.
Results. We find about 400 good candidate members ranging from OB types down to slightly subsolar masses. About 100 heavily reddened early-type Carina members found here were previously unrecognized or poorly classified, including two candidate O stars and several candidate Herbig Ae/Be stars. Their large brightness makes them useful tracers of the obscured Carina population. The spectroscopically derived temperatures for nearly 300 low-mass members enables the inference of individual extinction values and the study of the relative placement of stars along the line of sight.
Conclusions. We find a complex spatial structure with definite clustering of low-mass members around the most massive stars and spatially variable extinction. By combining the new data with existing X-ray data, we obtain a more complete picture of the three-dimensional spatial structure of the Carina clusters and of their connection to bright and dark nebulosity and UV sources. The identification of tens of background giants also enables us to determine the total optical depth of the Carina nebula along many sightlines. We are also able to put constraints on the star formation history of the region with Trumpler 14 stars found to be systematically younger than stars in other subclusters. We find a large percentage of fast-rotating stars among Carina solar-mass members, which provide new constraints on the rotational evolution of pre-main-sequence stars in this mass range.

Key words. stars: pre-main sequence – stars: early-type – open clusters and associations: individual: Trumpler 14 – open clusters and associations: individual: Trumpler 16 – open clusters and associations: individual: Carina nebula

⋆ Based on observations collected with the FLAMES spectrograph at VLT/UT2 telescope (Paranal Observatory, ESO, Chile), for the *Gaia*-ESO Large Public Survey (program 188.B-3002).

⋆⋆ Full Tables 1, 2, and 7 are only available at the CDS via anonymous ftp to cdsarc.u-strasbg.fr (130.79.128.5) or via http://cdsarc.u-strasbg.fr/viz-bin/qcat?J/A+A/603/A81

1. Introduction

The Carina nebula is one of the most massive H_{II} regions known in the Galaxy. It contains a large population of massive OB stars (the Car OB1 association), several Wolf-Rayet stars, and the well-known LBV star η Carinae. Most of the stellar content of the Carina nebula is found concentrated in a few clusters, notably Trumpler 16 (Tr 16, hosting η Car itself) and Trumpler 14 (Tr 14), about 10′ NNW of η Car. Less conspicuous clusters associated with the nebula include Trumpler 15, Collinder 228, and Collinder 232. The distance to η Car has been precisely determined to be 2.35 ± 0.05 kpc (Smith 2006). Car OB1 contains some of the most massive O stars known, including rare examples of O3 and even O2 stars. The properties of the region were reviewed by Smith & Brooks (2007, 2008). More recently, the whole Carina star formation region (SFR) was thoroughly investigated by means of a mosaic of Chandra X-ray observations (CCCP: Chandra Carina Complex Project; Townsley et al. 2011, and all papers in the series), after earlier X-ray studies of the central clusters Trumpler 16 and 14 with both Chandra (Albacete-Colombo et al. 2008) and *XMM-Newton* (Antokhin et al. 2008). X-ray data have been crucial to demonstrate the existence of a population (both clustered and diffuse) of ≥14 000 stars, undoubtedly associated with the SFR, which are most likely low-mass young stars formed in the nebula several millions years ago. Detailed studies of the stellar population in Carina have until now been exclusively directed toward characterizing its rich massive-star members, while there have been very few studies of its lower mass population. For example, DeGioia-Eastwood et al. (2001) reported optical photometry for only ∼850 stars in Trumpler 16 and 14. Deep optical photometry on more than 4500 stars in the same region was published by Hur et al. (2012) only fairly recently, allowing optical counterparts of faint X-ray sources to be studied. Spectroscopic studies of the low-mass PMS stars in these clusters are almost entirely lacking; Vaidya et al. (2015) present low-resolution spectra of 11 PMS stars.

The study of low-mass PMS stars at the distance of Carina, and sometimes embedded within obscuring dust and/or bright nebular emission, is time consuming and technically challenging. At the same time, it is important to test whether the early evolution of stars under such extreme ambient conditions, dominated by the presence of hundreds OB stars, differ from that in quieter SFRs (e.g., Taurus-Auriga or also Orion). Recent results from X-ray and IR surveys suggest that stars formed in rich clusters (e.g., Carina, Cygnus X, NGC 3603, and Westerlund 1 and 2) may be an important, if not dominant, component of all stars in the Galaxy, thus more representative of the average Milky-Way star than stars formed in less rich SFRs, such as Tau-Aur, Chamaeleon or IC348 (see, e.g., Lada and Lada 2003). Therefore, the study of Carina stars across the whole mass spectrum is likely to be relevant for a better understanding of the general stellar population in the Galaxy.

It is not clear whether the various clusters in Carina are coeval, and if not, whether this can be attributed to triggered or sequential star formation processes. Evidence for triggered formation in Carina have been discussed by Smith et al. (2010), but these authors focused on a different part of the nebula (the southern pillars) than that studied here; there is some overlap in the Tr 16 SE obscured region alone. In the central part of Carina studied here, evidence for recent or ongoing star formation is less frequent than in the southern parts (Povich et al. 2011b). Among the central Carina clusters, Tr 14 was suggested to be 1–2 Myr younger than Tr 16 because of its more compact structure and other characteristics (Walborn 1995; Smith 2006). It is however unclear if Tr 16 can still be considered a single cluster with a rather sparse population or rather as several physical clusters, as suggested by the X-ray results of Feigelson et al. (2011).

We present the first spectroscopic study of a sizable population of hundreds lower mass stars down to approximately one solar mass, using data from the *Gaia*-ESO Survey (Gilmore et al. 2012; Randich et al. 2013), to complement the studies of massive stars in Carina and obtain a more complete understanding of the star formation processes that have taken place in its recent past. The same observational dataset was used in a previous work (Damiani et al. 2016, Paper I) to study the dynamics of the ionized gas in the Carina H_{II} region from optical nebular emission lines.

This paper is structured as follows: in Sect. 2 we describe the composition of the observed sample; Sect. 3 discusses cluster membership for the observed stars; Sect. 4 discusses massive stars that happen to fall within our sample; Sect. 5 discusses the spatial clustering of stars; Sect. 6 is devoted to a discussion of reddening; Sect. 7 presents color–magnitude diagrams; Sect. 8 compares results from the present data with those from X-ray data; Sect. 9 discusses the structure of the whole region; Sect. 10 discusses stellar ages; and Sect. 11 the rotational properties of Carina stars. Eventually, we summarize our results in Sect. 12.

2. Observations and data analysis

2.1. Observed sample

We study a set of spectra of 1085 distinct stars in the Carina nebula, which was obtained with the FLAMES/Giraffe multi-fibre spectrometer at the ESO VLT/UT2 telescope on April 6–9, 2014 and released as part of the iDR4 *Gaia*-ESO data release. The total number of individual spectra was 1465, but all spectra relative to the same star were coadded to improve signal-to-noise ratio (S/N). Simultaneously, spectra with the FLAMES/UVES high-resolution spectrograph were obtained, which will be presented separately (Spina et al., in prep.). All spectra considered here are taken using Giraffe setup HR15n ($R \sim 17\,000$, wavelength range 6444–6818 Å), as in all *Gaia*-ESO observations of cool stars in open clusters. The (known) OB stars in Carina are instead observed using different Giraffe setups to obtain a more comprehensive set of diagnostics, which are better suited to hot stars; the massive star spectra are not part of the current data release and will be studied in a later work. As a consequence, we are only able to give a rough classification for the early-type stars that happen to fall within the sample studied here. The approach for deriving stellar parameters for later spectral types was instead described in Damiani et al. (2014) and Lanzafame et al. (2015).

The basis for our FLAMES target selection was the optical photometry published by Hur et al. (2012). This study covered a field, approximately 25′ × 25′ in size, comprising only the central portions of the entire nebula, and thus limited to the large clusters Tr 16 and 14 and the less rich Collinder 232. Moreover, with the HR15n setup, we did not observe stars brighter than $V = 12$, i.e., massive stars, observed with different Giraffe setups, nor fainter than $V = 18.5$ in order to obtain an acceptable minimum S/N. Since low-mass stars in the Carina SFR have not yet arrived on the zero-age main sequence (ZAMS), we also excluded stars in that region of the color–magnitude diagram (CMD). Also a spatial region near the edge of the photometric field of view, apparently dominated by field stars, was not observed, and finally, a random sampling of the remaining stars was performed to avoid an exceedingly long target list. This

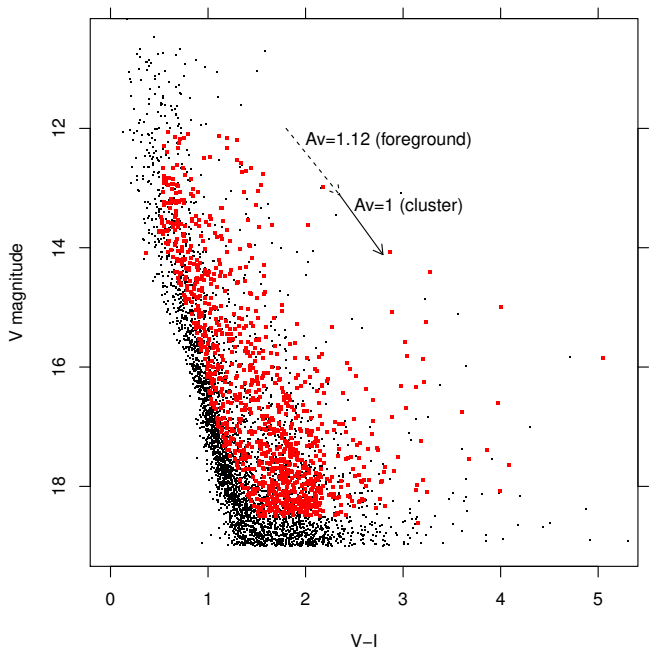

Fig. 1. (V, $V-I$) diagram of all stars in the Hur et al. (2012) catalog. Big red dots indicate the spectroscopically observed stars studied here. The dashed arrow indicates the foreground reddening vector, while the solid arrow indicates a representative intracluster reddening vector corresponding to $A_V = 1$.

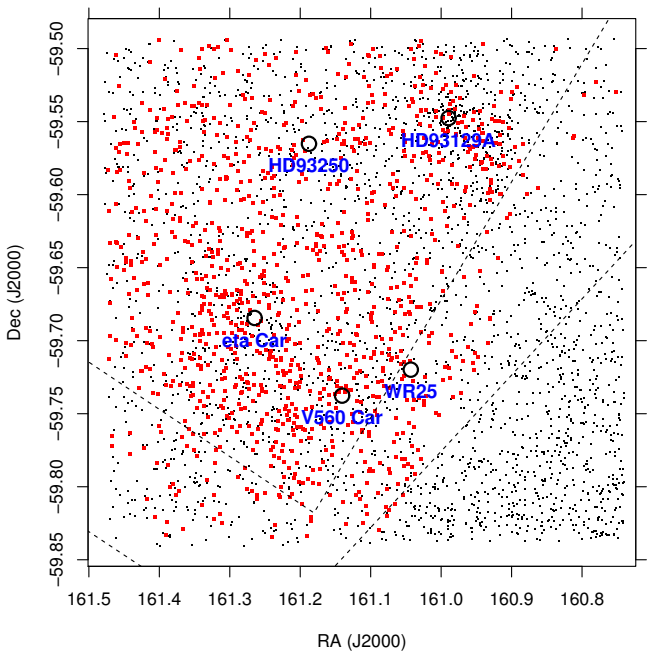

Fig. 2. Spatial distribution of Hur et al. (2012) stars brighter than $V = 18.5$ and of observed stars (red). The most massive stars in the region are indicated with big circles and names. The dashed lines indicate the approximate positions of the dark obscuring dust lanes bounding Tr 14 and 16.

procedure follows the general strategy for target selection in the *Gaia*-ESO Survey described in Bragaglia et al. (in prep.). The CMD of both the Hur et al. (2012) input catalog and our spectroscopically observed stars is shown in Fig. 1. Figure 2 shows instead the spatial distribution of input and observed stars. The median S/N of our 1085 spectra is 36.2.

2.2. Data analysis

The *Gaia*-ESO Survey data analysis process is distributed among several working groups, whose task is to apply homogeneous procedures to all datasets to ensure a high degree of internal coherence. As explained in Paper I, however, the Carina nebula presents a number of unanticipated features that are not dealt with accurately using standard procedures/pipelines; these features include the spatially nonuniform sky continuum level from reflection nebulosity and the wide Hα wings from both high-velocity ionized gas and reflection in the nebula. This required us to take a step back and redo part of the analysis, especially regarding a more appropriate subtraction of the sky spectrum, as described in the following. All derived parameters used here are released in the internal *GESiDR4* data release, database table *AstroAnalysis*. This reports the detailed results from each analysis node and their merged values produced by the relevant Working Group (WG12 in our case); because of the mentioned difficulties, results obtained from individual nodes sometimes using nonstandard, ad hoc procedures were preferred to WG12 results in the case of stellar parameters (from node "OAPA") and of lithium equivalent widths (EW; node "OACT"), while radial and rotational velocities were taken as those produced by WG12 (or node OAPA when these latter were missing).

The details of the special background-subtraction procedure employed by the OAPA node before evaluating stellar parameters are given in Appendix A. In short, after having separately corrected all atmospheric sky features, nebular lines are corrected using each of the nearest five sky spectra: the range of corrections obtained is an estimate of the uncertainty involved in the procedure, while the median of the five corrected spectra is taken as the best estimate stellar spectrum, for stellar parameter derivation. Lithium EWs were computed by different nodes, with results in good mutual agreement, using slightly different methods as explained in Lanzafame et al. (2015); the EW set from the OACT node was chosen because of its largest sample coverage. The WG12 radial and rotational velocities include contributions from both the OACT node, using methods detailed in Frasca et al. (2015), and OAPA node, using cross-correlation as briefly described in Damiani et al. (2014); a very good agreement is found for stars in common.

With the collection of five-fold nebular-subtracted stellar spectra obtained as explained in Appendix A, we proceeded with our estimates of stellar parameters (done five times per star), using the method explained in Damiani et al. (2014). This latter was purposely developed to deal with the spectral range and resolution of Giraffe HR15n data, and defines a set of spectral indices and their calibration to derive $T_{\rm eff}$, $\log g$, and [Fe/H] for stars later than ∼A2. The range spanned by each parameter in its own set of five determinations corresponds to the systematic error introduced by sky correction, which is often larger than the statistical error. Depending on the intensity ratio between the nebular Hα wings and stellar Hα wings, these latter may in some cases be exceedingly affected by nebular emission and cannot be used as a temperature diagnostic, for example in A to mid-G stars[1]. For mid-A to lower mass stars, fortunately, other indicators may be used to estimate temperatures (although the increased dependence on metallicity must be treated with caution). The problem is worst for early-A stars, where almost the only spectral line in HR15n range is Hα. Much weaker lines

[1] The most important features of stellar spectra in the HR15n wavelength range are described in Damiani et al. (2014).

are found in the blue extreme of the HR15n range, where grating efficiency is however very low, and are therefore difficult to use in low-S/N spectra. In practice, many faint early-A stars are recognized in the Tr 14/16 dataset as those having a nearly flat, featureless continuum spectrum with indefinite properties in the Hα region because of the predominant nebular emission. B-type stars are instead easily recognized because of their He I 6678 Å line. The He I nebular line at the same wavelength usually has no wings (Paper I) and is much narrower than the stellar line, often broadened by fast rotation.

The wide nebular Hα wings are also of great nuisance when trying to select stars with intrinsic wide Hα emission owing to accretion from a circumstellar disk (e.g., classical T Tauri stars, CTTS, or Herbig Ae/Be stars, HAeBe). Here again, the five-fold nebular-subtracted star spectra are of invaluable help in separating cases where the apparent wide emission in the net spectrum arises from poorly subtracted nebular Hα wings (as it will not be present in all five net spectra) from truly wide Hα lines of CTTS/HAeBe stars.

2.3. Auxiliary datasets

The stellar population of the Carina nebula was the object of several recent studies. We have therefore cross-matched our spectroscopic targets with objects in several existing catalogs. A match with the CCCP X-ray source catalog (Broos et al. 2011a) yielded 352 matches among our 1085 sample stars. The match was made assuming a constant 1σ error on optical positions of 0.2 arcsec, individual catalogued X-ray position errors, and a 4σ maximum distance. The number of spurious matches was estimated as 13, by artificially shifting one of the two position lists by ±1 arcmin. Then we considered the VPHAS+ DR2 Point Source Catalogue (Drew et al. 2014) with photometry in the bands *ugri* and Hα. Using a maximum matching distance of 5σ, and constant position errors of 0.2 arcsec for both optical and VPHAS+ catalogs, we obtain 1074 matches (of which ∼140 estimated as spurious). However, the number of stars with a *clean* = *yes* photometric flag in all of *r*, *i*, and Hα bands, matching our target list, is of only 171. Last, we similarly matched our targets to the young stellar object (YSO) catalog of Zeidler et al. (2016), obtained from both VISTA and *Spitzer* near/mid-IR data. The number of matches is 64 (∼1 spurious), of which however only 7 have catalogued magnitudes in all four *Spitzer* IRAC bands (3.6−8.0μ). All of these latter were already members by spectroscopic criteria; see below.

3. Cluster membership

Since the chosen sample-selection strategy for *Gaia*-ESO Giraffe observations is inclusive of most possible members, the membership of observed stars to each cluster must be determined ex post facto. Since our emphasis is on young, low-mass stars (FGK stars), the most useful membership indicators are the lithium line EW and strong X-ray emission in addition to radial velocity (RV) as usual. Wide Hα emission wings, which are indicative of circumstellar accretion in pre-main-sequence (PMS) stars, provide strong evidence of extreme youth and probable membership to a SFR, even in the absence of a RV measurement (e.g., in cases of strong-emission stars without observable photospheric absorption lines). As described above, a star must show wide Hα emission consistently across the multiple (five) sky-subtraction options to be considered a reliable CTTS/HAeBe. This conservative approach undoubtedly misses some real emission-line members, but is a minor issue for building a reliable member list since the other membership criteria may compensate for this. Narrow, chromospheric Hα emission cannot be used as a youth indicator because it is swamped by the nebular emission lines no matter which sky-subtraction option is chosen. In order to minimize the number of spurious members, a star is generally accepted as member only when it satisfies at least two criteria among: $|RV - RV_0| < \Delta RV$ (with RV_0 and ΔRV to be determined), lithium $EW > 150$ mÅ, X-ray detection, and CTTS/HAeBe status. However, since each of these criteria may include significant numbers of contaminants (e.g., G stars up to an age of about 1 Gyr would fall above our lithium EW threshold), some additional screening was applied, as described below.

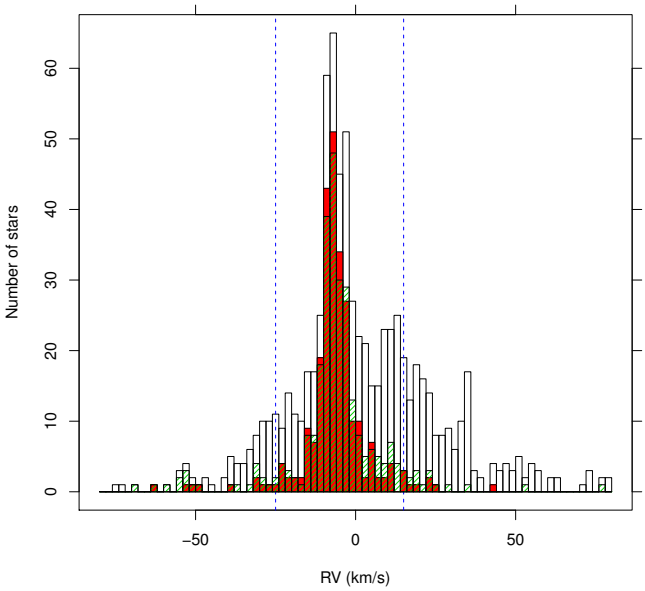

Fig. 3. Histogram of (heliocentric) RV for all stars with $T_{\rm eff} < 8800$ K and $S/N > 15$ (white-colored bars). The red filled histogram represents stars with lithium $EW > 150$ mÅ; the dashed green histogram are stars detected in X-rays. The vertical dashed blue lines at $RV = (-25, +15)$ indicate our fiducial limits for RV membership.

To help determine RV_0 and ΔRV, Fig. 3 shows a histogram of RV for stars with $T_{\rm eff} < 8800$ K (and $S/N > 15$). Colored histograms refer to lithium- and X-ray-selected candidates; these indicators select essentially the same population of low-mass Carina members. From this figure, we find that good values for RV_0 and ΔRV are −5 and 20 km s^{-1}, respectively; the latter is chosen to be rather inclusive since additional indicators are also used for final membership assessment[2]. According to the above-stated general rule, inside the dashed RV limits only one membership criterion (the RV criterion being fulfilled) is sufficient to consider a star a member; outside of these limits, at least two indicators are needed. The number of stars shown in the total histogram is 755; scaled to this number, we expect nine spurious optical X-ray matches to be included in these histograms, distributed uniformly *per star* (not *per RV interval*). Therefore, most of the spurious X-ray matches lie inside the dashed lines, where most stars are found. This justifies in part several bins containing X-ray detections in excess of lithium-rich stars. For

[2] The value of mean radial velocity RV_0 is in good agreement with that of the local molecular gas; see, e.g., Rebolledo et al. (2016, their Fig. 5), with heliocentric $RV_0 = -5$ km s^{-1}, corresponding to $V_{\rm LSR} = -13.8$ km s^{-1}.

the same reason, we expect 6–7 contaminants among candidate members found only from RV and X-ray criteria.

A handful of stars satisfying the general membership criteria above are found in the CMD very near the ZAMS at the cluster distance (or, in any case, at apparent ages >20 Myr according to Siess et al. 2000 isochrones), even after accounting for reddening as in the following sections. Upon individual examination, only two[3] of these 17 stars showed strong enough indications of membership to be retained in our list, while the others, mostly low-S/N spectra with poorly constrained parameters, were removed. Of these latter, 6 were simultaneously RV- and X-ray members, in very good agreement with their expected number.

Among our targets, we searched for additional candidate CTTS members, but did not find any candidates by looking in other catalogs, such as the VPHAS+ data, in particular, using the $(r-i, r-\mathrm{H}\alpha)$ diagram locus as in Kalari et al. (2015); the 2MASS data; and finally the *Spitzer* data from Broos et al. (2011a; table 6), considering disk-bearing stars with colors $[3.6-4.5] > 0.2$ and $[5.8-8.0] > 0.2$. To this stage, the number of low-mass candidate Carina members (colder than ~8000 K) found is 303, of which approximately 150 are candidate CTTS.

We find also many stars with $T_{\rm eff}$ above 6500 K, which already at this young age have no traces of lithium and are sometimes rotating so fast that an accurate derivation of RV might not be possible. Moreover, it is known that A-type stars are not strong coronal X-ray emitters (e.g., Schmitt 1997), such that our member list is least reliable for stars earlier than type F (approximately $T_{\rm eff} \geq 7000$ K). Early-A and B-type stars, of which we find several tens, are instead rare in the field, so that most of them can be safely considered as Carina members (adding to the 303 low-mass candidates), even though their RVs might sometimes not be accurately determined because of fast rotation.

A more detailed examination of candidate members is performed from their cumulative RV distribution, as shown in Fig. 4. The black curve is the RV cumulative distribution for all single member stars with $T_{\rm eff} < 7000$ K, $v \sin i < 50$ km s^{-1}, and $S/N > 15$ (177 stars). A cumulative Gaussian distribution fitted to the median RV range between $(-20, 40)$ km s^{-1} is shown with the green curve (maximum-likelihood parameters $\langle RV \rangle = -5.9$ km s^{-1}, $\sigma(RV) = 4.66$ km s^{-1}). However, an obvious asymmetry is present between the two tails of the Gaussian distribution with an excess of stars at $RV > 0$ km s^{-1}. Unrecognized binaries are only expected to produce symmetric tails. We inspected all spectra of stars with $RV > 0$, to check that no RV determination errors were present to a level that might justify the observed discrepancy. The red curve therefore shows the cumulative distribution corresponding to two superimposed Gaussians with maximum-likelihood parameters as follows: $\langle RV_1 \rangle = -7.07$ km s^{-1}, $\sigma(RV)_1 = 3.48$ km s^{-1} and $\langle RV_2 \rangle = 7.81$ km s^{-1}, $\sigma(RV)_2 = 6.37$ km s^{-1}. The main Gaussian distribution accounts for 77% of stars in the subsample considered here. The still misfit tail at $RV \sim -20$ km s^{-1} may be attributed to either binaries or an additional small population, of 6–7 stars, which was not examined further. The ~40 stars in the positive-velocity Gaussian are too numerous to be explained by spurious X-ray matches, whose number was quantified above. Therefore, they are likely genuine X-ray bright and/or lithium rich stars or young stars in general. Their discrepant RV distribution with respect to the main Carina population does not entitle us to consider them Carina members. Based on their approximate RV, we refer to these stars as "RV10 stars". There are 29 RV10 stars with $RV > 3$ km s^{-1}, $T_{\rm eff} < 7000$ K, $v \sin i < 50$ km s^{-1}, and $S/N > 15$.

We investigate the nature of the RV10 group by means of the $T_{\rm eff}$-lithium EW diagram (Fig. 5). The RV10 stars account for most of the low-lithium candidate members; however, more than

[3] These are the candidate HAeBe star [HSB2012] 2504 and the star [HSB2012] 2692, showing strong lithium, IR excess in the 2MASS bands, and an association with a YSO.

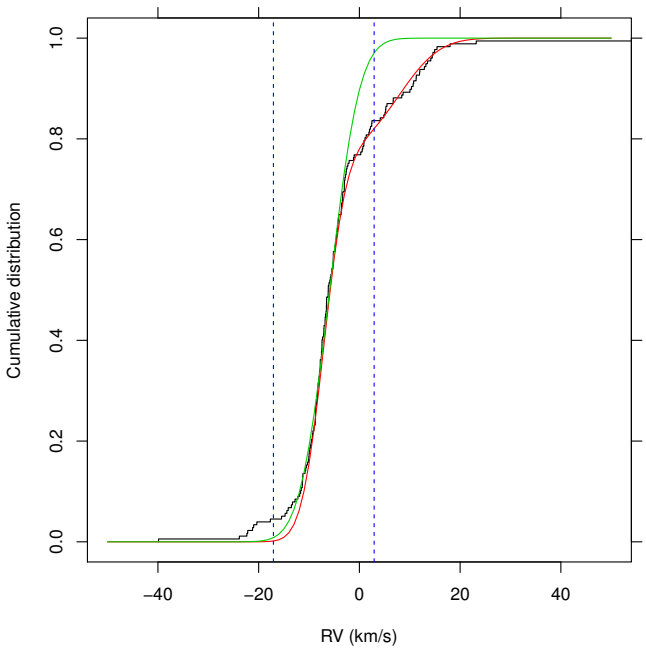

Fig. 4. Cumulative RV distribution for late-type members with $T_{\rm eff} < 7000$ K and $v \sin i < 50$ km s^{-1} (solid line). The green line indicates a cumulative single-Gaussian distribution; the red line indicates a double-Gaussian distribution. The blue vertical dashed lines indicate ±7 km s^{-1} from median RV, as a reference.

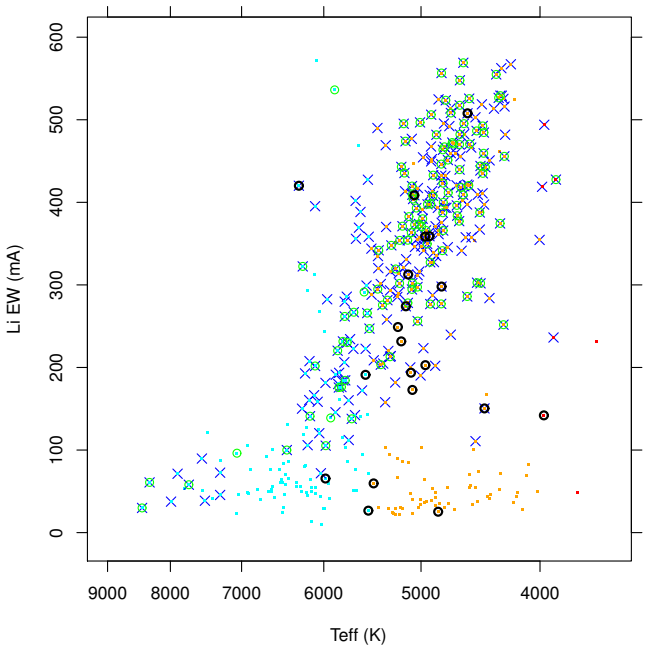

Fig. 5. Diagram of lithium EW vs. $T_{\rm eff}$. Color-coding of small dots corresponds roughly to solar mass and earlier-type stars (cyan), late-G to mid-K stars (orange), and M-type stars (red). Probable members are indicated with blue crosses. Green circles indicate (CTTS or Herbig Ae/Be) stars with wide Hα emission. The bigger black circles indicate RV10 stars.

Table 1. Identifications for late-type Carina members.

HSB2012	CXOGNC	ADM2008	YSO	RA (J2000)	Dec (J2000)	V	$B-V$	$V-I$
796	...	...	...	10:43:31.96	−59:33:56.4	16.36	0.93	1.15
800	104332.23-593511.3	...	...	10:43:32.25	−59:35:11.5	16.20	0.80	1.11
908	104336.77-593315.2	...	...	10:43:36.77	−59:33:15.2	14.72	0.68	1.17
907	...	...	...	10:43:36.77	−59:36:48.2	17.12	1.10	1.19
954	104338.76-593301.9	...	...	10:43:38.80	−59:33:01.8	16.21	1.08	1.50
953	104338.81-593423.7	...	...	10:43:38.80	−59:34:23.8	18.19	...	2.33
995	104340.13-593356.0	...	104340.14-593356.3	10:43:40.13	−59:33:56.1	18.32	...	2.09
998	104340.19-593449.5	...	...	10:43:40.18	−59:34:49.6	17.04	1.55	2.13
1035	104341.45-593352.7	...	...	10:43:41.45	−59:33:52.8	13.33	0.73	1.14
1051	104341.97-593352.6	...	...	10:43:41.90	−59:33:53.0	17.86	...	1.86

Notes. Column HSB2012 reports the identifier in Hur et al. (2012); column CXOGNC is the identifier in Broos et al. (2011a); column ADM2008 is the identifier in Albacete-Colombo et al. (2008); column YSO is the identifier in Zeidler et al. (2016). V magnitudes, $B-V$ and $V-I$ colors are from Hur et al. (2012). Full table is available at the CDS.

Table 2. Parameters of late-type Carina members.

HSB2012	S/N	RV (km s^{-1})	$v \sin i$ (km s^{-1})	$T_{\rm eff}$ (K)	A_V	Li EW (mÅ)	γ	log age (yr)	Hα	SB2
796	17.0	2.5± 2.5	20.3± 3.3	5694±218	0.75	137.8±12.0	1.01±0.015	...	Y	N
800	43.1	−0.7± 6.2	74.2± 8.1	5978± 95	0.81	105.3± 6.4	1.009±0.006	...	Y	N
908	62.5	−11.5± 7.4	30.0±12.7	7541± 92	1.77	89.7± 3.9	0.999±0.004	...	N	N
907	28.5	−4.9± 0.6	13.6± 1.7	4869± 95	0.31	202.0± 6.6	0.969±0.009	6.98	N	N
954	49.6	−6.5± 8.0	69.0± 2.7	5727± 67	1.52	160.3± 6.3	1.01±0.005	...	N	N
953	25.9	−3.6± 1.4	24.8± 1.5	4865±104	2.78	371.0± 8.3	1.022± 0.01	6.30	N	N
995	16.6	−6.8± 2.0	13.0± 1.6	5019±172	2.44	373.8±11.0	0.999±0.016	...	Y	N
998	47.0	−9.3± 7.0	92.4± 1.4	4942± 60	2.44	349.6± 7.4	1.011±0.006	6.12	Y	N
1035	130.4	−0.7±15.1	99.4± 9.6	7498± 43	1.67	38.6± 2.3	0.998±0.002	...	N	N
1051	18.2	−5.2± 2.0	15.0± 0.5	5177±159	2.04	371.1± 7.9	1.028±0.015	6.89	Y	N

Notes. Column HSB2012 reports the identifier in Hur et al. (2012). S/N is the spectrum median signal/noise ratio. RV is the heliocentric radial velocity. Errors on $T_{\rm eff}$ are statistical only. The gravity index γ is defined in Damiani et al. (2014). Column "log age" is the photometric age. Column Hα reports "Y" if an excess Hα emission is detected, either from accretion (CTTS) or chromospheric, distinct from the nebular Hα emission. Column "SB2" is "Y" for SB2 binaries. Full table is available at the CDS.

one-half of the RV10 stars have Li $EW > 150$ mÅ and follow the same relation with $T_{\rm eff}$ as Carina members, which are apparently coeval. All RV10 stars with Li $EW > 250$ mÅ have extinction (as determined in Sect. 6) higher than the foreground $A_V^{\rm fg}$ toward Carina (Hur et al. 2012). Nearly one-half of the RV10 stars have instead low extinction, suggesting that they are foreground stars; at the same time, many of these stars have significant Li EWs, indicating they are young stars (say <100 Myr) in agreement with their frequent X-ray detection (18/29 stars). The spatial distribution of RV10 stars does not show clustering and their location on the optical CMD often does not overlap the main cluster locus. We conclude that the RV10 are dominated by a group of (17) foreground young stars, unrelated to the Carina cluster, probably spanning a significant age range, and characterized by a common dynamics. Also their $v \sin i$ distribution is typical of young low-mass stars. We therefore speculate that they are a remnant from a now dissolved cluster, closer to us than the Carina nebula, in the same sky direction.

The 12 RV10 stars with $A_V > A_V^{\rm fg}$ are instead probable Carina low-mass members, whose net number becomes 286. Among these stars we find 8 SB2 binaries; this appears to be a low percentage compared to other studies (e.g., Mathieu 1994); however, fast rotation, frequently found among Carina members (see Sect. 11) may render double-lined systems more difficult to detect, so we cannot draw firm conclusions on this subject for Carina stars. We do not consider these SB2 stars in the rest of the paper. The identifications and properties of Carina members are listed in Tables 1 and 2, while those of the RV10 group are in Tables 3 and 4.

Three stars with strong lithium lines, but showing no other membership indicator, turned out to be nonmember lithium-rich giants, upon a detailed examination of their stellar parameters. Their identifications and properties are reported in Tables 5 and 6.

4. Massive stars

Our observed sample selection was made with the aim of studying low-mass stars in Carina, starting from A-type stars. However, a number of earlier-type stars are serendipitously found among the spectra studied here. Those O-type and B-type stars are intrinsically more luminous than the rest of the sample, but some were included here because of their higher extinctions or, in some cases, because they are located at significantly larger distances; the Carina nebula is close to the tangent of a spiral arm. Although HR15n spectra are not ideal for a detailed classification of hot stars, we attempt here to assign a qualitative classification of these stars, whose importance in the study of the

Table 3. Identifications of RV10 stars.

HSB2012	CXOGNC	ADM2008	YSO	RA (J2000)	Dec (J2000)	V	$B-V$	$V-I$
394	104314.98-593341.3	...	...	10:43:14.99	−59:33:41.3	14.67	0.94	1.09
1262	104348.74-593430.4	...	...	10:43:48.59	−59:34:31.2	17.72	1.76	2.03
1788	104405.37-593043.5	...	...	10:44:05.42	−59:30:43.5	14.53	0.90	1.03
2169	...	...	...	10:44:18.67	−59:48:05.4	16.09	0.96	1.02
2270	...	...	...	10:44:22.78	−59:38:52.5	18.44	...	1.75
2296	104423.64-593941.8	146	...	10:44:23.56	−59:39:41.4	16.34	0.91	1.34
2561	...	...	...	10:44:32.97	−59:38:05.9	17.38	0.94	1.22
2797	...	...	...	10:44:42.77	−59:38:01.4	17.03	1.14	1.14
2959	104450.11-593429.3	...	...	10:44:49.99	−59:34:29.5	16.75	1.32	1.72
3030	104452.43-594130.1	469	...	10:44:52.40	−59:41:30.1	16.66	0.94	1.15
3167	104457.05-593826.5	534	...	10:44:57.06	−59:38:26.9	13.70	1.01	1.19
3229	...	...	...	10:44:58.90	-59:40:08.4	15.66	1.18	1.27
3290	104501.02-594515.5	600	...	10:45:01.03	−59:45:15.6	14.54	0.91	1.06
3688	...	...	...	10:45:15.44	-59:35:21.4	17.29	1.48	1.81
3844	104521.23-593258.2	...	...	10:45:21.20	−59:32:58.4	18.06	1.26	1.63
3926	104524.13-593131.1	...	...	10:45:24.14	−59:31:31.6	14.20	0.63	0.71
4310	104541.60-593820.2	1014	...	10:45:41.60	−59:38:20.2	14.46	0.87	1.00

Notes. Columns as in Table 1.

Table 4. Parameters of RV10 stars.

HSB2012	S/N	RV (km s^{-1})	$v \sin i$ (km s^{-1})	$T_{\rm eff}$ (K)	A_V	Li EW (mÅ)	γ	log age (yr)	Hα	SB2
394	31.1	10.3±1.1	24.0± 0.5	5189±105	0.39	231.6±7.2	0.984±0.009	...	N	N
1262	30.6	13.2±1.6	10.9± 2.5	3830± 17	0.42	...± ...	0.862±0.008	...	Y	N
1788	84.4	23.2±0.4	12.0± 0.5	5082± 38	0.20	172.8±3.1	0.984±0.003	...	N	N
2169	40.1	14.2±0.6	13.9± 1.6	5095± 76	0.19	193.7±5.2	0.985±0.007	...	N	N
2270	17.4	4.8±2.5	17.9±10.0	3816± 25	0.00	...± ...	0.847±0.015	...	Y	N
2296	59.0	15.4±2.2	18.7± 1.5	5548± 66	1.10	191.1±5.3	1.012±0.004	...	N	N
2561	31.7	14.6±0.9	12.0± 0.5	4731± 73	0.21	...± ...	0.974±0.008	...	Y	N
2797	42.1	14.9±1.1	12.3± 2.4	5115± 69	0.45	...± ...	0.988±0.006	...	Y	N
2959	41.4	92.5±2.7	27.0± 0.5	4295± 40	0.64	...± ...	0.984±0.006	...	Y	N
3030	42.5	10.8±1.3	24.0± 2.7	5465± 84	0.67	59.6±5.4	1.001±0.006	...	N	N
3167	112.9	10.7±0.7	15.0± 0.5	4842± 26	0.29	25.3±1.6	0.992±0.002	...	N	N
3229	68.3	4.1±0.7	12.0± 0.5	5519± 50	0.94	26.6±2.7	0.994±0.004	...	Y	N
3290	65.5	8.7±2.0	45.0± 0.5	4959± 44	0.16	202.8±4.4	0.98±0.004	...	N	N
3688	30.9	11.3±1.2	10.4± 1.7	4124± 41	0.51	...± ...	0.85±0.008	...	Y	N
3844	16.7	6.7±1.4	12.0± 0.5	3971± 54	0.00	142.0±9.3	0.92±0.016	...	Y	N
3926	28.6	8.4±1.0	9.6± 2.6	5981±137	0.00	65.5±6.1	0.978±0.009	...	N	N
4310	59.3	10.0±1.0	21.0± 0.5	5221± 56	0.22	249.0±4.0	0.986±0.004	...	N	N

Notes. Columns as in Table 2.

Table 5. Identifications of lithium-rich field giants.

HSB2012	CXOGNC	ADM2008	YSO	RA (J2000)	Dec (J2000)	V	$B-V$	$V-I$
3579	...	...	...	10:45:11.09	−59:40:07.8	15.85	1.96	5.05
2595	...	...	...	10:44:34.42	−59:42:57.8	15.87	2.49	3.20
3504	...	...	...	10:45:08.53	−59:43:30.2	18.10	...	3.25

Notes. Columns as in Table 1.

Carina SFR cannot be neglected. The spectroscopic information is complemented with a study using archival photometry.

4.1. Spectroscopic analysis

As mentioned in Sect. 2, the HR15n wavelength range contains the He I 6678.15 Å line, which is a very useful diagnostic to select B-type stars. Of course, care must be used since at nearly the same wavelength a Fe I line is found in cooler stars, so that establishing a B-type spectrum also requires absence of metallic lines and in particular of the group of lines between 6490–6500 Å (Damiani et al. 2014), which are strong enough to remain recognizable even in fast rotators. As explained in Sect. 2 above (and see Paper I for details), Hα and He I lines, which are

Table 6. Parameters of lithium-rich field giants.

HSB2012	S/N	RV (km s^{-1})	$v \sin i$ (km s^{-1})	$T_{\rm eff}$ (K)	A_V	Li EW (mÅ)	γ	log age (yr)	Hα	SB2
3579	133.3	22.1 ± 2.3	24.7 ± 4.6	2819 ± 24	...	487.5 ± 2.1	1.019 ± 0.002	...	N	N
2595	96.9	17.7 ± 1.4	18.9 ± 1.6	3598 ± 150	2.20	231.3 ± 2.1	1.061 ± 0.003	...	N	N
3504	32.0	43.1 ± 0.7	7.5 ± 1.7	4424 ± 69	4.24	167.5 ± 5.9	1.051 ± 0.008	...	N	N

Notes. Columns as in Table 2.

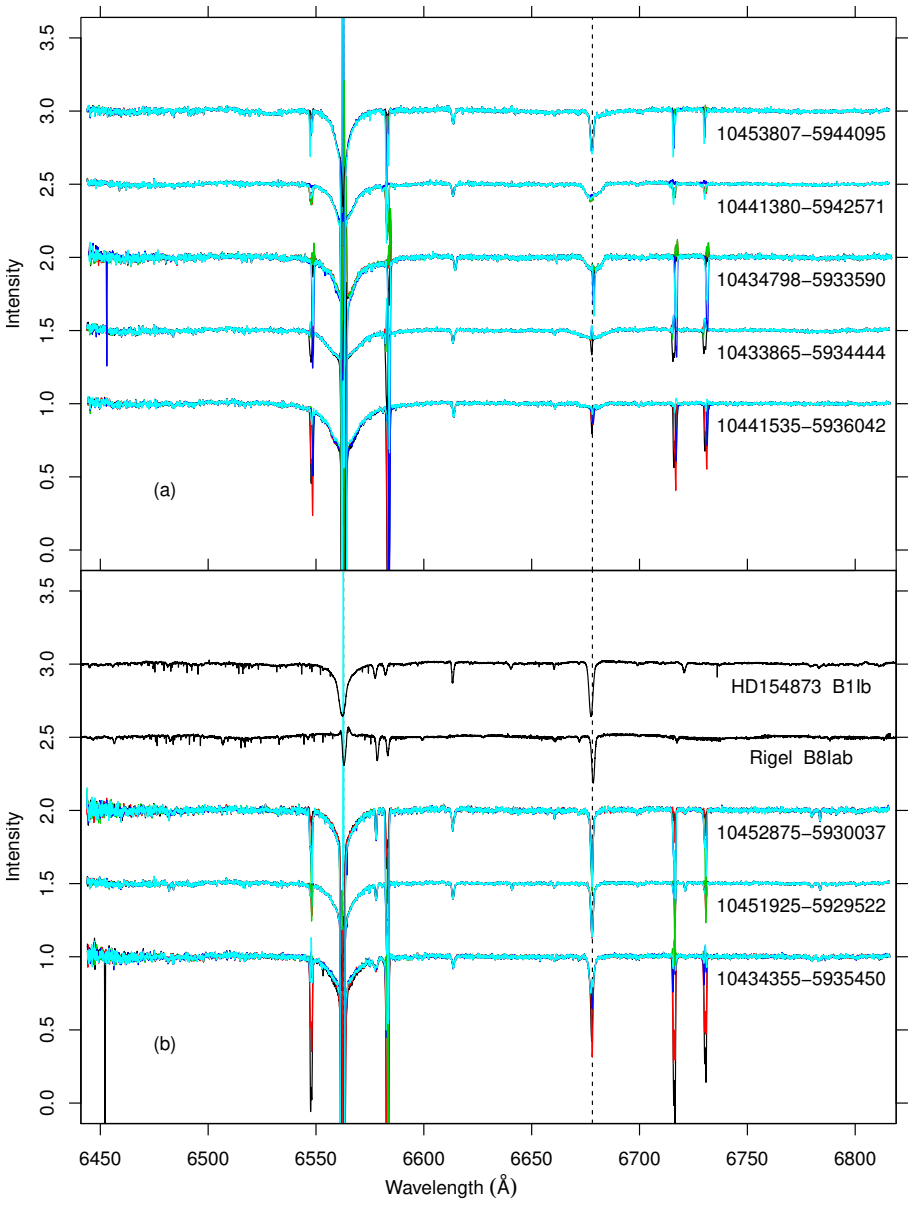

Fig. 6. *Top* **a)** example spectra of B stars found among our targets. For each star, five spectra are overplotted with different colors, corresponding to five distinct options regarding nebular subtraction. The vertical dashed black line indicates the He I 6678 Å line, distinctive of B stars, but also coincident with a strong, narrow nebular line. Spectra of different stars are offset by 0.5 for clarity. The narrow absorption feature near 6613 Å is a well-known DIB, while a weaker DIB is sometimes visible near 6660 Å. *Bottom* **b)** spectra of sample B stars (lower three spectra) showing absorption in the C II doublet near 6580 Å (the redder line in the doublet coincides with the nebular [N II] 6584 Å line), which is typical of known B bright giants/supergiants (upper two spectra, from UVES/POP). The vertical dashed lines indicate Hα and He I 6678 Å.

the most intense lines in the HR15n range for late-B stars, and the only detectable at low S/N, are both coincident with nebular sky lines, whose contribution is often impossible to subtract accurately. Therefore, classification of late-B stars on the basis of the present data may only be approximate. In practice it is often impossible to confirm or exclude the presence of a weak He I line in the spectrum of a fast-rotating star without metallic lines to discriminate between a late-B and an early-A type and, therefore, we assign to these stars a generic "late-B/early-A" type. In tens of other cases, He I is safely detected, but again nebular lines make the determination of the stellar He I EW unreliable; these stars were thus classified as "B-type" without better detail. Examples of B-type stars in our dataset are shown in Fig. 6a. In this figure, differences in the adopted sky correction are evident only in the cores of nebular lines Hα, [N II] 6548, 6584 Å, He I, and [S II] 6717, 6731 Å.

Some of the B stars show a characteristic C II doublet at 6578–6583 Å, which is typical of mid-B stars, but is enhanced in bright giants or supergiants (Grigsby et al. 1992; Sigut 1996; McErlean et al. 1999). We therefore consider these stars candidate B supergiants, although some of them may be

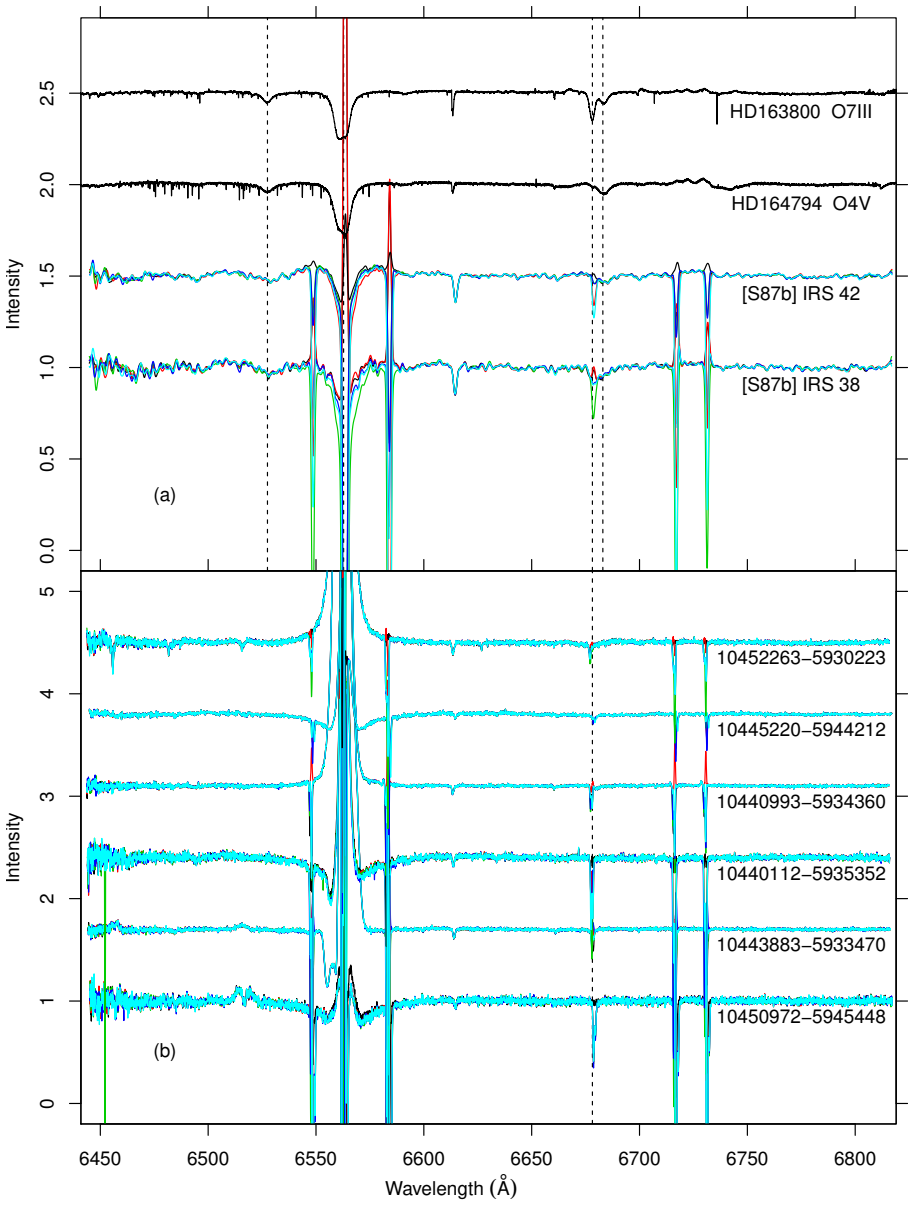

Fig. 7. *Top* **a)** spectra of a possible O star (SIMBAD identifier [S87b] IRS 38), a probable O star ([S87b] IRS 42), and two UVES/POP spectra of known O stars. The lower two spectra were slightly smoothed to improve their visibility. Dashed vertical lines indicate Hα and He I 6678 Å, as above, plus the He II lines at 6527 and 6684 Å, typical of O stars. *Bottom* **b)** example spectra of new candidate Herbig Ae/Be stars discovered in this work.

main-sequence B stars as well. We show some of these spectra in Fig. 6b, together with spectra of two known B supergiants (top two spectra) from the UVES/POP dataset (Bagnulo et al. 2003).

The *Gaia*-ESO spectra of two of our stars show features suggesting an O stellar type: these are the He II lines at 6527 Å and 6683 Å. Their spectra are shown in Fig. 7a (bottom two spectra), compared with known O stars from UVES/POP. The intensity ratio between He I 6678 Å and the neighboring He II 6683 Å line would be a sensitive measure of spectral type; however, the nebular contamination at 6678 Å is strong for both stars, since they are highly reddened and faint, which prevents accurate derivation of their spectral types. Furthermore, a large percentage of OB stars are spectroscopic binaries (Sota et al. 2014) and an examination of these lines in the sample covered by spectroscopic surveys such as OWN (Barbá et al. 2010), IACOB (Simón-Díaz et al. 2011), or CAFÉ-BEANS (Negueruela et al. 2015) reveal a number of cases where a B+B SB2 (each star with a He I 6678 Å line) masquerades as a single object with both He I and He II lines. Finally, He II 6527 Å is close to a broad DIB. Therefore, their identification as O stars based on their spectra is tentative at this stage. Both stars have already appeared in the literature on Carina stars, first as bright IR sources in Smith (1987; the corresponding designation is reported in Fig. 7a), then as candidate massive stars from both X-ray and IR observations (Sanchawala et al. 2007; Povich et al. 2011a); no optical spectra were however published for these stars before.

Finally, 17 stars are good or possible candidates as Herbig Ae/Be stars with an A/B type and definite (regardless of sky-subtraction option chosen) wide emission at Hα. We show some examples of these stars' spectra in Fig. 7b. Some of the spectra also show absorption or emission in the Fe II lines at 6456.38, 6516.08 Å, indicative of hot gas. While many of the spectra of these stars clearly show wide Hα absorption wings, underlying the circumstellar Hα emission, in some cases the absorption component is overwhelmed by the wide emission component. In these cases the HAeBe nature is suggested by either a He I line, by the Fe II lines, or by the optical photometry when this is more consistent with an A-B type than with a lower mass CTTS.

All massive stars found in our spectral dataset are listed in Table 7. The "SIMBAD Id" column shows that all of these stars have also appeared in the SIMBAD database; however, for only

Table 7. Early-type stars.

2MASS Id	SIMBAD Id	RA	Dec	V	$B-V$	$V-I$	SpT	Notes
10430716-5931209	[HSB2012] 230	10:43:07.16	−59:31:20.9	15.06	1.08	1.76	...	B type
10432086-5929595	[HSB2012] 538	10:43:20.86	−59:29:59.6	14.43	0.39	0.72	...	B type
10433865-5934444	Cl Trumpler 14 43	10:43:38.66	−59:34:44.5	12.17	0.42	0.71	...	B type
10434798-5933590	Cl Trumpler 14 45	10:43:47.98	−59:33:59.1	13.2	0.44	0.73	...	B type
10435224-5936585	[HSB2012] 1385	10:43:52.24	−59:36:58.5	12.24	0.4	0.7	...	B type
10435250-5942503	[HSB2012] 1395	10:43:52.50	−59:42:50.4	16.47	1.1	1.8	...	B type
10435723-5932411	Cl* Trumpler 14 VBF 65	10:43:57.24	−59:32:41.2	12.85	0.31	0.55	...	B type
...	[HSB2012] 1618	10:43:59.20	−59:33:21.5	13.44	0.39	0.67	...	B type
10440320-5937380	Cl* Trumpler 14 Y 461	10:44:03.20	−59:37:38.1	12.67	0.3	0.54	...	B type
10440384-5933099	Cl Trumpler 14 38	10:44:03.84	−59:33:10.0	13.23	0.34	0.55	...	B type

Notes. Column "SpT" reports the spectral type listed in SIMBAD. Column "Notes" reports our classification, in particular: "B SG" indicates candidate B supergiants; "HAeBe" indicates Herbig Ae/Be stars; "near A0" indicates stars of late-B/early-A type. Full table is available at the CDS.

Table 8. Results of the CHORIZOS fits for the 7 highly extinguished stars with $UBVIJHK$ photometry.

Star	$T_{\rm eff}$ kK	LC	R_{5495}	$E(4405-5495)$ mag	$\log d$ pc	A_V mag	$\chi^2_{\rm red}$
[HSB2012] 3017	22.2 ± 2.5	5.0	3.62 ± 0.08	1.291 ± 0.039	3.50 ± 0.07	4.688 ± 0.077	1.9
[HSB2012] 230	41.8 ± 5.3	5.0	3.95 ± 0.07	1.393 ± 0.023	3.88 ± 0.11	5.531 ± 0.036	0.8
[HSB2012] 1395	42.3 ± 5.2	5.0	4.20 ± 0.08	1.384 ± 0.022	4.11 ± 0.11	5.831 ± 0.040	0.7
[HSB2012] 2913	40.8 ± 6.0	5.0	3.69 ± 0.05	1.828 ± 0.026	3.85 ± 0.12	6.756 ± 0.040	0.2
[HSB2012] 3994	18.5 ± 3.2	1.0	4.57 ± 0.10	1.290 ± 0.045	4.51 ± 0.05	5.902 ± 0.114	3.7
[S87b] IRS 41	42.4 ± 4.4	5.0	4.92 ± 0.09	1.351 ± 0.020	3.37 ± 0.09	6.669 ± 0.034	6.4
[S87b] IRS 42	42.0 ± 4.2	5.0	4.60 ± 0.06	1.932 ± 0.021	3.22 ± 0.09	8.860 ± 0.033	11.3

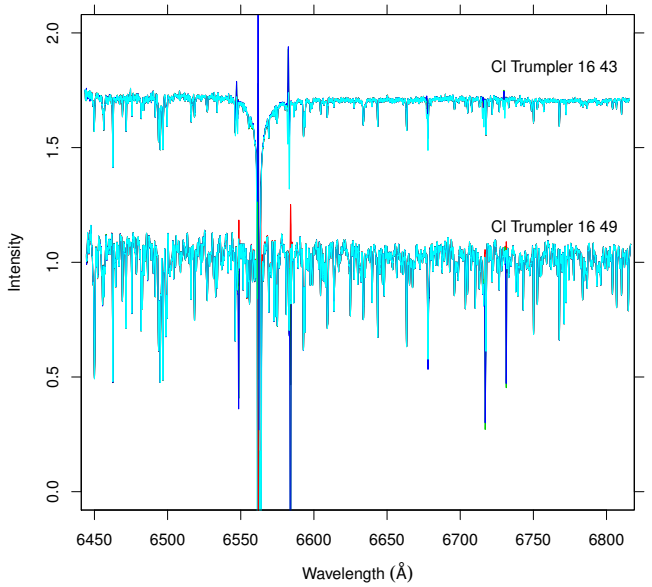

Fig. 8. Spectra of two stars misclassified in the SIMBAD database as B stars, while they are a K giant (*lower* spectrum), and a late-A or F star (*upper* spectrum), respectively. Spectra are labeled with their SIMBAD identifier. Color coding as in Fig. 6.

12 of them a B spectral type was already determined. Therefore, the large majority of our early-type stars are new entries in the massive-star population of Carina, including all HAeBe stars. Incidentally, our complete spectral sample also includes two stars for which SIMBAD lists a B spectral type (with no reference given), while our spectra show definitely later (F and K) spectral types, as shown in Fig. 8.

We have also matched our stellar sample with the lists of candidate massive stars from Sanchawala et al. (2007) and Povich et al. (2011a). Of the 7 matches with the Sanchawala et al. (2007) candidates, we confirm a type earlier than early-A for 4 (at most 5) stars; only 4 of our stars match the Povich et al. (2011a) candidates and all of them are confirmed as early-type stars. The combined list contains 11 massive star candidates, of which only 2–3 are not confirmed. Again, these are small numbers with respect to the number of new early-type stars found for the first time in our *Gaia*-ESO spectra (110 stars in Table 7) in a spatial region much smaller than the whole Carina region covered by the Povich et al. (2011a) study.

4.2. Photometric analysis with CHORIZOS

Some of the massive stars identified in this section are potentially interesting because their colors suggest large extinctions ($A_V \sim 5$ or higher), which are rarely found for objects immersed in H II regions. For that reason we selected 10 stars from Table 7 that are potential candidates for being highly extinguished. For 7 of the stars $UBVIJHK$ photometry is available from Hur et al. (2012) and 2MASS (Table 8), while for the remaining 3 only $BVIJHK$ photometry exists (Table 9).

We processed the photometry described above using the CHORIZOS code (Maíz Apellániz 2004) to measure the extinction experienced by the stars and, to the degree in which it is possible, their effective temperature $T_{\rm eff}$ and logarithmic distance $\log d$. The procedure followed is similar to that used in other papers such as Maíz Apellániz et al. (2015). With the purpose of obtaining independent assessments of the properties

Table 9. Results of the CHORIZOS fits for the three highly extinguished stars with *BVIJHK* photometry.

Star	R_{5495}	$E(4405-5495)$ mag	A_V mag	$\chi^2_{\rm red}$
[HSB2012] 3880	3.64 ± 0.06	2.106 ± 0.030	7.636 ± 0.040	1.4
[HSB2012] 1920	3.93 ± 0.06	2.238 ± 0.030	8.757 ± 0.026	4.6
[S87b] IRS 38	4.07 ± 0.05	2.825 ± 0.030	11.394 ± 0.034	30.4

of these stars, the results from the spectroscopic analysis above were not used as inputs here. We start by providing details of the *UBVIJHK* photometry case as follows:

- We used the Milky Way grid of Maíz Apellániz (2013a), in which the grid parameters are the effective temperature ($T_{\rm eff}$) and photometric luminosity class (LC). The latter quantity is defined in an analogous way to the spectroscopic equivalent, but maps discrete classes I–V to a continuous variable in the range [0–5.5]. For objects with $T_{\rm eff} > 15$ kK the spectral energy distributions (SEDs) are TLUSTY (Lanz & Hubeny 2003).
- The extinction laws were those of Maíz Apellániz et al. (2014), which are a single-family parameter with the type of extinction defined by R_{5495} (monochromatic analogous of R_V, see Maíz Apellániz 2013b). The amount of reddening is parameterized by $E(4405-5495)$.
- LC was fixed to 5.0 (main sequence) in all cases except for [HSB2012] 3994, for which it was fixed to 1.0 (supergiant). The values $T_{\rm eff}$, R_{5495}, $E(4405-5495)$, and $\log d$ were left as free parameters.

The *BVIJHK* photometry case was similar but it required an additional step. The problem with lacking *U*-band photometry is that $T_{\rm eff}$ and $\log d$ become quasi-degenerate (even if LC is known). R_{5495} and $E(4405-5495)$, however, are strongly constrained, as the different combinations of valid $T_{\rm eff}$ and $\log d$ yield almost identical values of the two extinction parameters. Therefore, the procedure we followed was to select a reasonable fixed value of $\log d$ and leave $T_{\rm eff}$, R_{5495}, and $E(4405-5495)$ as free parameters.

The results of the CHORIZOS analysis are presented in Tables 8 and 9.

- We find values of R_{5495} between ≈3.6 and ≈4.9, which are higher than the Galactic average but typical for an H II region.
- $E(4405-5495)$ ranges between ≈1.3 and ≈2.8, reflecting the known strong differential extinction. The three stars with no *U*-band photometry have the three highest values of $E(4405-5495)$, as expected.
- Typically, A_V is determined with better precision than either R_{5495} or $E(4405-5495)$ even though, to a first approximation, $A_V \approx R_{5495} \cdot E(4405-5495)$. This is not incorrect because the likelihood in the R_{5495}–$E(4405-5495)$ plane is an elongated quasi-ellipsoid with negative slope, i.e., R_{5495} and $E(4405-5495)$ are anticorrelated. This effect is commonly seen in fits to extinguished hot stars with CHORIZOS or similar codes.
- The most important result regarding the extinction is the location of four stars ([S87b] IRS 41, [S87b] IRS 42, [HSB2012] 1920, and [S87b] IRS 38) in the $E(4405-5495)$-R_{5495} plane. A comparison with Fig. 2 of Maíz Apellániz (2015) reveals that they are in a region where no other known Galactic OB stars are located. That is because for low values of $E(4405-5495)$, it is possible to find a large range of R_{5495} values but for large reddenings R_{5495} tends to be close to the average ∼3.1 value. In other words, those four stars are exceptional in having large values of both $E(4405-5495)$ and R_{5495}, and their extinctions laws deserve a more detailed study.
- We plot in Fig. 9 the dependence of $\chi^2_{\rm red}$ of the CHORIZOS fit with reddening. For $R_{5495} < 4.0$, the fits are reasonably good even for values of $E(4405-5495) \sim 2.0$, indicating the validity of the extinction laws of Maíz Apellániz et al. (2014) for low R_{5495}. For $R_{5495} > 4.0$, there are good fits for low values of the reddening but $\chi^2_{\rm red}$ grows increasingly large as $E(4405-5495)$ increases, indicating that the extinction laws of Maíz Apellániz et al. (2014) need to be modified for large values of R_{5495}. This is not surprising, given that those laws were derived using stars with lower reddenings and here we are extrapolating to much larger values.
- For two of the B-type stars (as determined from the spectroscopy) with *UBVIJHK* photometry ([HSB2012] 3017 and [HSB2012] 3994), the CHORIZOS-derived $T_{\rm eff}$ is consistent with their being mid-B stars. For the other five objects with *UBVIJHK* photometry (from the spectroscopy, three B types, one B SG, and one O type), the uncertainties in $T_{\rm eff}$ are larger and the values lean toward their being O stars. However, we should be cautious of that result, especially for the cases with high $\chi^2_{\rm red}$. They could be late-O stars (with weak He II 6683 Å) or the fitted values for $T_{\rm eff}$ could be biased by the extinction law (Maíz Apellániz et al. 2014).

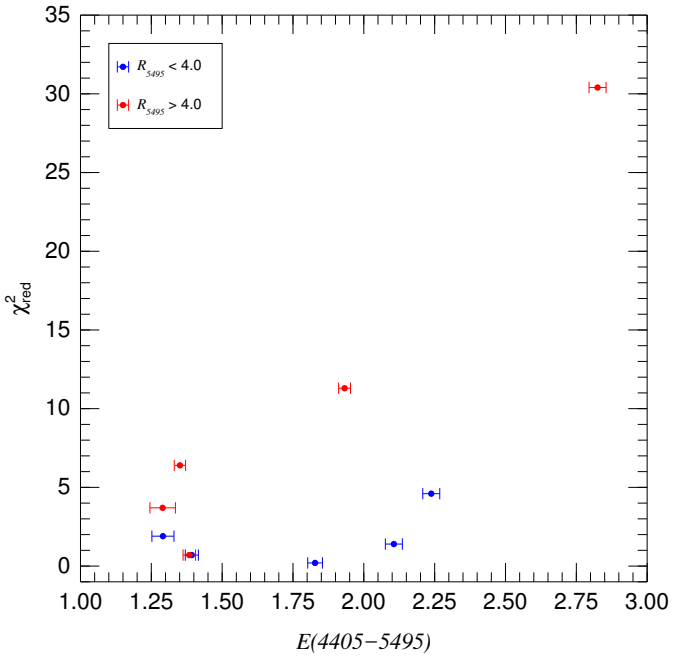

Fig. 9. $\chi^2_{\rm red}$ vs. $E(4405-5495)$ for the 10 highly extinguished stars analyzed with CHORIZOS.

– [HSB2012] 3994 has an exceptionally large fitted distance (beyond the expected extent of the Galactic disk). One possible solution is that it is not a supergiant but instead a lower luminosity star. Even then, it is likely to lie beyond the Carina nebula.
– Three other stars ([HSB2012] 230, [HSB2012] 1395, and [HSB2012] 2913) are also likely to lie beyond the Carina nebula. On the other hand, the fitted $\log d$ for [HSB2012] 3017, [S87b] IRS 41, and [S87b] IRS 42 are compatible with them belonging to the Carina nebula association. It should be pointed out that the latter list includes the two stars with the highest values of R_{5495}. That is an expected effect because for stars beyond the Carina nebula one expects a larger contribution to extinction from the diffuse ISM and, hence, a lower R_{5495}.

The uncertainties derived by CHORIZOS are relatively small but not unrealistic because for over a decade we have worked to eliminate the systematic errors that have plagued other works. That includes recalculating the zero points for different photometric systems (Maíz Apellániz 2005, 2006, 2007), complementing and testing different atmosphere grids (Maíz Apellániz 2013a), deriving a new family of extinction laws that provides significant better fits to photometric data than pre-existing ones (Maíz Apellániz 2013b; Maíz Apellániz et al. 2014), obtaining a library of data on reference stars to serve as a test bed for all of the above (Maíz Apellániz et al. 2004, 2011; Maíz Apellániz & Sota 2008), and integrating everything into the code.

5. Spatial groups

The Carina nebula is known to host a morphologically complex stellar population, distributed among approximately 20 subclusters and a sparse population, according to Feigelson et al. (2011), of which Tr 14 and Tr 16 are only the most massive. Therefore, we define several spatial groupings into which we conveniently split our sample stars. Among clusters defined in Feigelson et al. (2011), numbers 1, 3–6, 9–12, 14 fall in the region studied here. This is however a too detailed subdivision considering the number of optical spectra available here, so we prefer a simpler categorization. In Fig. 10 we show the spatial distribution of all stars observed in *Gaia*-ESO and known massive stars as a reference. The most massive stars are also coincident with the brightest X-ray sources (see Fig. 1 in Antokhin et al. 2008) and exert the strongest influence on their neighborhood. Accordingly, we define five spatial regions, delimited by red dashed segments in the figure, centered on stars HD 93129A (O2If*+O2If*+O:, central star of Tr 14), V560 Car (=HD 93205, O3.5V((f+))+O8V), HD 93250 (O4IIIfc:, central star of Collinder 232), WR25 (=HD 93162, O2.5If*/WN6), and η Car.

6. Reddening

Determination of optical extinction toward individual stars is very important to establish how they are distributed along the line of sight. A number of studies (e.g., Smith 1987; Hur et al. 2012) have determined that the foreground extinction toward Carina is relatively low ($E(B-V) \sim 0.36 \pm 0.04$, or $A_V^{\rm fg} \sim 1.1$), while higher reddening stars in the same region show an anomalous reddening law with $R = 4.4$–4.8. In the central part of Carina being studied here, highly obscured member stars have been found by means of X-ray observations (Albacete-Colombo et al. 2008; CCCP). Therefore, even considering only Tr 14/16 (and not the embedded clusters of Feigelson et al. 2011), cluster members are found over a large range of extinction values. The spatially highly nonuniform distribution of extinction is also made obvious by the two prominent SE and SW dark dust lanes.

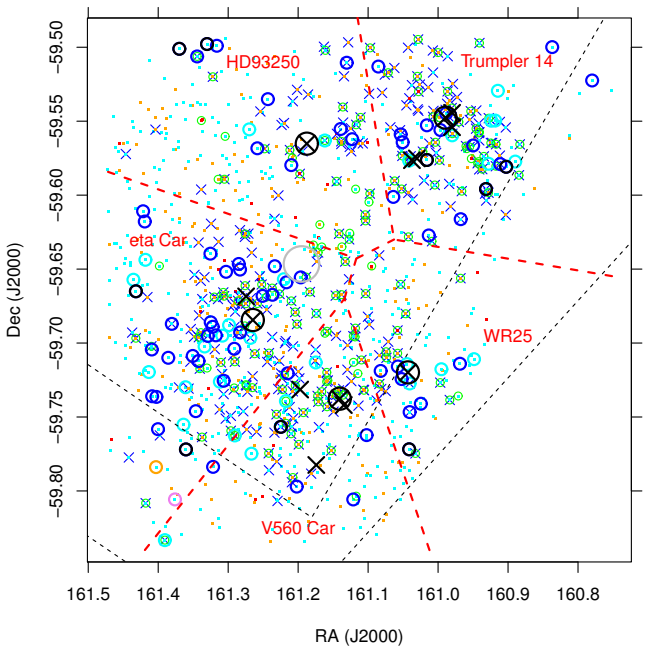

Fig. 10. Spatial map of observed stars. The lower right region is empty because of our sample selection choice. Symbols as in Fig. 5, with the addition of big circles to indicate B stars (blue), late-B to early-A stars (cyan), candidate B supergiants (black), and probable (orange) or possible (violet) O stars. We also plot O stars from Walborn (1973) as black crosses. The most massive of these stars (surrounded by big black circles) are taken as centers of the respective subregions, bounded by red dashed lines, and labeled in red after the central star names (except for Trumpler 14, whose central star is HD 93129A). Dashed black segments delimit the dark V-shaped dust lanes in front of the nebula. The solid gray circle to the NW of η Car indicates approximate location and size of the Keyhole nebula (Smith & Brooks 2008).

Figure 11 shows a $(B-V, V-I)$ color-color diagram (using photometry from Hur et al. 2012), where in particular the colors of the early-type stars (large circles) found from our spectroscopy are useful to study the intracluster reddening law. The intrinsic colors of massive stars (down to A0) are described by the red line (3-Myr nonrotating solar-metallicity isochrone from Ekström et al. 2012, henceforth Geneva[4]), while those of lower mass stars by the gray line (ZAMS from Kenyon & Hartmann 1995; henceforth KH95). Despite the lack of a detailed classification for the massive stars (Sect. 4), it is expected that most of them are late-B or early-A stars with colors $B-V \sim V-I \sim 0$. On this basis, the slope of the dashed arrow in Fig. 11 suggests that the foreground reddening law is $E(V-I)/E(B-V) = 1.53$, which is slightly larger than the value 1.32 in Bessell et al. (1998); inside Carina this ratio becomes 1.95 (slope of the black solid arrow), which is slightly larger than the value found by Hur et al. (2012) of 1.8 ± 0.1 from photometry alone. Fig. 11 also shows that some of the B-type stars redder than $B-V \sim 1$ appear to have a lower $E(V-I)/E(B-V)$ ratio, more like a normal reddening law, although their spatial distribution shows no obvious pattern. Moreover, the two candidate O stars found in Sect. 4 are both found at very large reddenings (orange and violet circles),

[4] http://obswww.unige.ch/Recherche/evoldb/index/Isochrone/

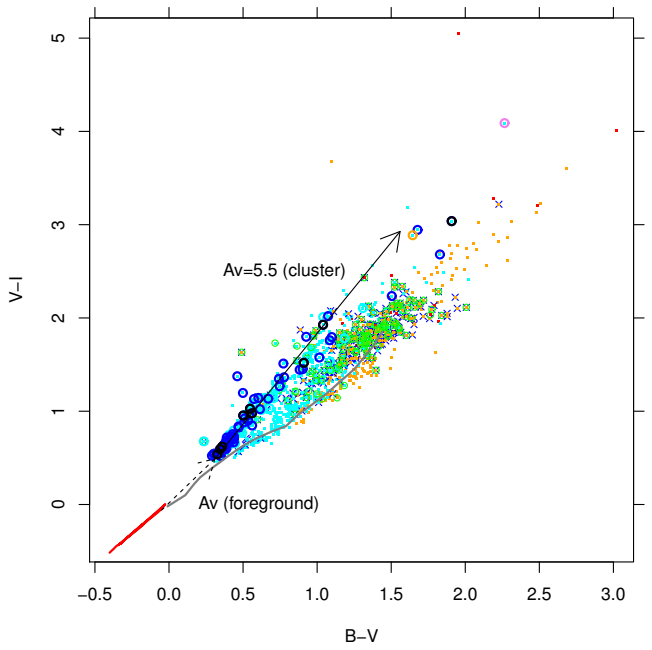

Fig. 11. ($B-V$, $V-I$) color–color diagram of the observed sample. Symbols as in Figs. 5 and 10. The thick red line indicates the unreddened locus of stars earlier than A0, while the thick gray line indicates the same for later type stars. The reddening law appropriate for cluster stars is illustrated by the solid arrow on top of the dashed arrow describing foreground absorption (and reddening law). The length of the solid arrow indicates the reddening of the new candidate O star 2MASS10453674-5947020 (star [S87b] IRS 42 in SIMBAD).

corresponding to intracluster extinction $A_V > 5.5$. Among stars with $B-V \geq 2$, the mentioned O star is the only candidate cluster member: the handful of other stars found in that color range are therefore obscured background giants, whose detection permits us to estimate the total optical extinction of the nebula, and its spatial variation, as we discuss below and in Sect. 9.

We determined individual extinction values for our stars from their photometric $V-I$ colors, $T_{\rm eff}$ derived from our spectroscopy, and the $T_{\rm eff}$-color relation from KH95 for ZAMS stars[5]; the $E(V-I)$ colors were converted to A_V using the above reddening laws as appropriate, i.e., differently for foreground extinction only ($A_V < 1.1$) and foreground+intra-cluster extinction, each with its reddening law. Because of our inability to assign a detailed spectral type and photometric color to the early-type stars, their extinction was computed by dereddening their photometry to match the 3-Myr isochrone from Ekström et al. (2012). Figure 12 shows $T_{\rm eff}$ versus $V-I$ diagrams for all of our stars separately for the different spatial groups (defined in Sect. 5). The solid line is the KH95 calibration at zero reddening, while the dashed line is the same curve at $A_V = A_V^{\rm fg} = 1.1$; it is clear that most low-mass cluster members fall a little to the right of the latter curve. In this figure we also show the placement of giant stars (defined from the γ index in Damiani et al. 2014) as red circles: as anticipated above, most of these giants lie at large reddening values[6] and likely beyond the Carina nebula. In the Trumpler 14 region virtually no background stars are seen: this might be related to a relatively higher extinction compared to other sightlines, and also to our incomplete target sampling combined with a locally enhanced member-to-field star density ratio.

7. Color–magnitude diagram

We show the dereddened CMD of our sample stars in Fig. 13. We find probable cluster members of masses down to one solar mass (or slightly below). The nonuniform reddening however prevents us from establishing a mass completeness limit; we cannot be sure of detecting even O stars (our candidate O star [S87b] IRS 38 has $V = 17.64$) in places where the reddening is largest. Nonuniform reddening causes bright stars to be over-represented among optically selected samples such as this one, hence we find a relatively large number of B stars relative to solar-mass stars in our sample. This dataset is therefore unsuitable for studies (e.g., of the IMF) requiring statistically representative samples. The scarcity of cluster members in the $(V-I)_0$ range 0.2–0.5, corresponding to late-A and F stars, is also apparent from the figure. The same lack of members can be observed in Fig. 12 at $T_{\rm eff}$ near 7000 K. Since lower mass stars are found in larger numbers, this cannot be due to excessive reddening toward the F stars. One possible explanation for the small number of F-type members is the relatively fast traversal time across their radiative tracks in the CMD. In addition, we might lack the ability to assess their membership, as mentioned already in Sect. 3 for the A-type stars. Since F-type stars are generally found to be as strong X-ray emitters as G-type stars, we consider them again in the context of the Carina X-ray data below.

Ages for the low-mass stars estimated from the isochrones in Fig. 13 are distributed mostly in the range 1–5 Myr, in agreement with previous studies (e.g., Tapia et al. 2003; Carraro et al. 2004; Hur et al. 2012). As noted by, for example Smith & Brooks (2008) or Wolk et al. (2011), not all clusters in Carina are the same age (Tr 14, in particular, is more compact and probably younger than Tr 16). The problem of establishing their age relationship is discussed in Sect. 10.

8. X-ray data

In the subregion comprising Tr 16 and WR25 we find approximately 180 low-mass candidate Carina members. Considering that our target selection involved a ~50% down-sampling of all candidate members from optical photometry down to $V = 18.5$, we can extrapolate to ~360 members down to that magnitude limit; this is much smaller than the number of X-ray sources (1035) found in the same region by Albacete-Colombo et al. (2008). An even larger number was found in the CCCP X-ray survey, even though this survey was based on the same Chandra observation in the field of Tr 16, because of the less conservative choices adopted in detecting point sources. Spurious detections in Albacete-Colombo et al. (2008) are predicted not to exceed ~10 sources and the number of unrelated field X-ray sources is ~100, so that the number of X-ray members in this subregion remains >900. Therefore, a significant excess of ≥500 X-ray sources remain, above the number of members inferred from our spectroscopic data. These must be stars fainter than our $V = 18.5$ selection limit, either because of their low mass or because of large extinction (or both). Since their number is not small with respect to the spectroscopically studied sample, we cannot overlook them for a proper understanding of the properties of the SFR. Here we try to investigate their nature.

[5] Although the KH95 relation may be superseded by more recent calibrations, its usage here for deriving A_V is appropriate for best consistency with the $T_{\rm eff}$ calibration in Damiani et al. (2014).

[6] The employed KH95 calibration is appropriate to ZAMS stars, and therefore the reddening values derived by applying it to giants are only approximate, but sufficient for our classification as background stars.

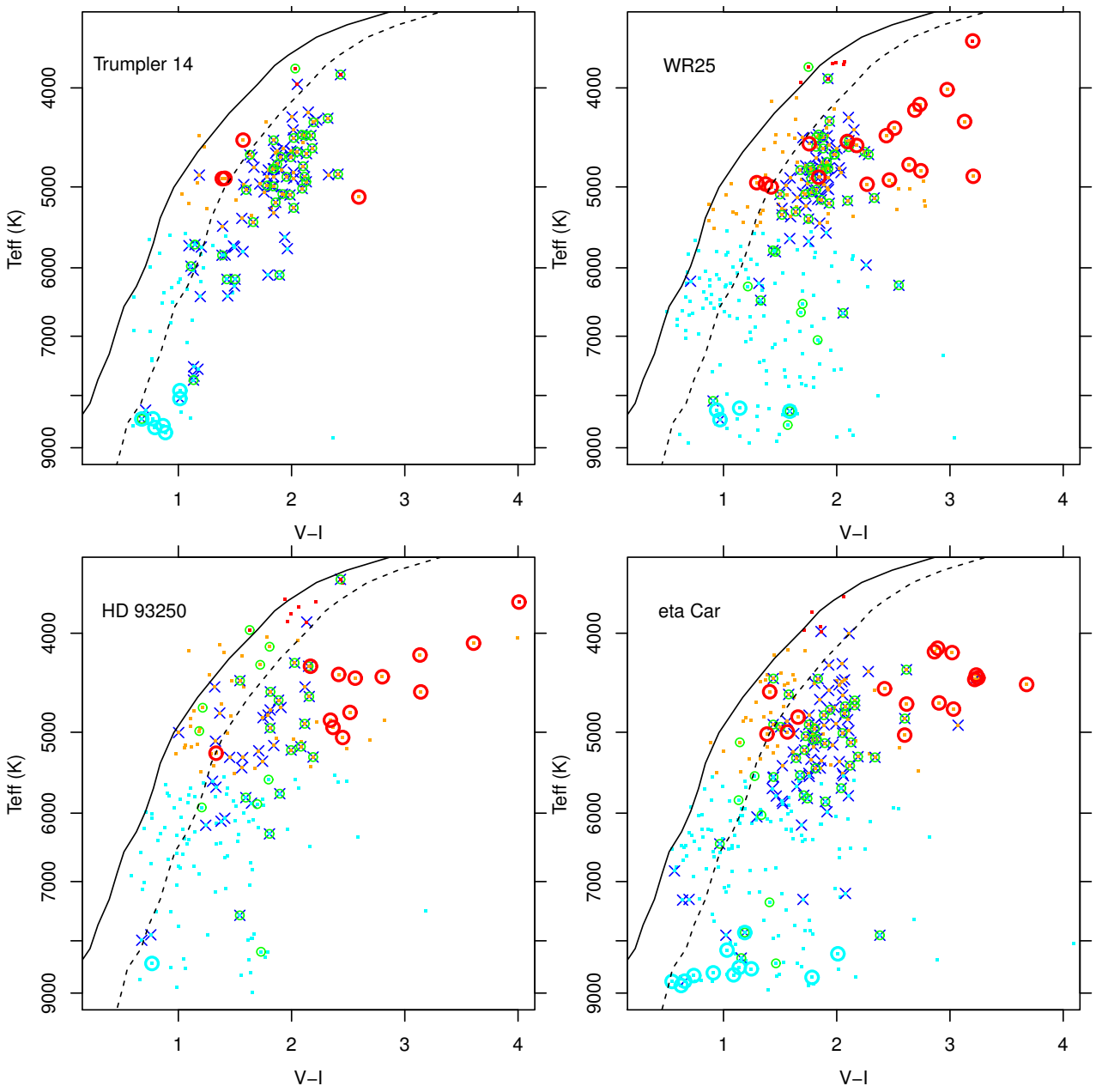

Fig. 12. Diagrams of $T_{\rm eff}$ vs. color $V-I$, for four spatial subregions as indicated. The KH95 $T_{\rm eff}$-color relation is shown for zero reddening (solid) and for the cluster foreground reddening (dashed). Symbols as in Figs. 5 and 10. Big red circles indicate luminous low-gravity giants, probably located behind the nebula.

Forty X-ray detected late-type stars (21 from Albacete-Colombo et al. 2008) were observed spectroscopically, but not classified here as members; of these stars, 11 are RV10 stars and 6 are near-ZAMS rejected members discussed in Sect. 3. We first examine whether this can reveal a failure of our membership criteria. These stars do not cluster at any particular place in the CMD diagram and there is no reason to conclude that as a group they should be included among members. The same conclusion is reached from Fig. 14, showing RV versus $T_{\rm eff}$ exclusively for nonmember stars: the X-ray emitting nonmembers are randomly scattered, and in particular their membership status would not change by any small adjustment of the nominal RV range for members (horizontal lines). We recall that, if these X-ray sources had lithium EW above 150 mA, they would have been accepted as members even in the presence of discrepant RV (in order not to lose binaries)[7]. Thus, the red crosses in Fig. 14 not only have discrepant RV but also no lithium. As discussed above, in the $T_{\rm eff}$ range 9000–7000 K our membership criteria may be weakest; yet, even in this range the number of potential candidates from X-rays is very small and they all appear to have significantly discrepant RV. Therefore, these X-ray detected stars with no lithium and discrepant RV are unlikely members and are not considered further[8]. We also conclude that the lack

[7] The few red crosses inside the nominal RV range were rejected as members because of their proximity to the ZAMS, as explained above.

[8] Of these 40 stars, 37 are classified by Broos et al. (2011b) within the CCCP project, on the basis of X-ray properties and optical-NIR photometry alone: all but four (unclassified) objects were assigned to the "Carina young star" group including, thus, the majority of near-ZAMS and RV10 stars, which we instead excluded on the basis of the Hur et al. (2012) photometry and our RVs, respectively.

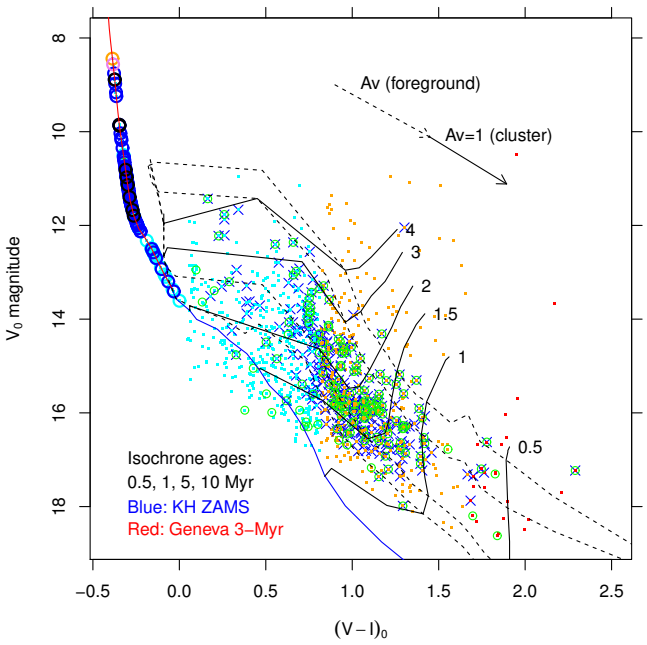

Fig. 13. Dereddened (V, $V-I$) color–magnitude diagram. Symbols as in Figs. 5 and 10. Also shown are the ZAMS for lower MS stars (blue), a Geneva 3-Myr isochrone for massive stars (red), and selected isochrones (dashed black) and evolutionary tracks (solid black) for lower mass stars from Siess et al. (2000); these latter are labeled with stellar mass in solar units. The A0 and earlier type stars have been projected to the MS (along the combined foreground + cluster reddening vector, as shown), since they lack a detailed classification.

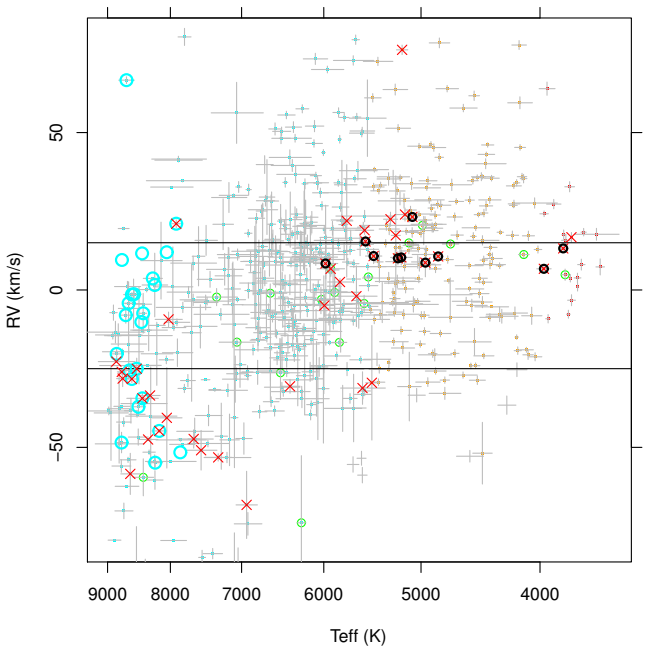

Fig. 14. Radial velocity vs. $T_{\rm eff}$ for stars not classified as members. Symbols as in Fig. 5, with the addition of red crosses representing X-ray detected stars, unconfirmed by other membership indicators. Bars indicate statistical errors only. The RV10 stars are indicated with black circles. The horizontal lines indicate the cluster RV range.

of member stars in the temperature range 9000–7000 K is real and not a byproduct of our membership criteria. This is probably related to the R-C gap found in the photometric CMD of several clusters by Mayne et al. (2007); the same effect is not recognizable in the CMD of Carina clusters because of strong differential extinction.

Next, we examine the X-ray properties of X-ray detected sources that have not been observed spectroscopically. We take the list of sources and their properties from Albacete-Colombo et al. (2008). Figure 15a compares cumulative distributions of extinction A_V (as derived from the near-IR colors for X-ray sources with a 2MASS counterpart), for the X-ray sources in the spectroscopic sample and in the no-spectroscopy sample. A Kolmogorov-Smirnov (KS) statistical test gives a probability P that the two distributions are drawn from the same parent sample of only $P = 4.9 \times 10^{-5}$, confirming the significance of their visually apparent difference. Similar results are obtained from consideration of the absorbing column density $N_{\rm H}$, as derived from model best fits to the Chandra ACIS X-ray spectra (Albacete-Colombo et al. 2008), whose distributions for the spectroscopically observed and unobserved samples of X-ray sources are also shown in Fig. 15a: here a KS test gives a probability of $P = 1.83 \times 10^{-6}$ that the two distributions are drawn from the same parent sample. The two tests just made do not refer to the exact same subsamples of X-ray sources, since only two-thirds of the X-ray sources in Albacete-Colombo et al. (2008) have a 2MASS counterpart and only those detected with more than 20 X-ray counts had a spectral fit performed. Nevertheless, there is definite evidence that the optically missed, X-ray detected members are more obscured than the stars in our spectroscopic sample.

This finding does not rule out that the X-ray detected sample may also contain a number of low-extinction members at fainter optical magnitudes than our limit. To test this, we considered the distributions of X-ray luminosities $L_{\rm X}$, derived from X-ray spectral fits and therefore corrected for absorption, for the spectroscopic and no-spectroscopy samples, as shown in Fig. 15b: the KS test gives a probability of no difference of $P = 2.2 \times 10^{-16}$. Young PMS low-mass stars are known to be in an X-ray saturated regime, where the X-ray luminosity $L_{\rm X}$ is on average proportional to stellar bolometric luminosity, $L_{\rm X} \sim 10^{-3} L_{\rm bol}$ (Flaccomio et al. 2003, Preibisch et al. 2005; Damiani et al. 2006a); therefore, the lower (unabsorbed) X-ray luminosities of stars without spectroscopy implies that these stars have on average lower luminosities (and mass) than our spectroscopic sample. The X-ray detected member sample is therefore more complete than the spectroscopic sample both toward lower masses and toward more obscured stars.

9. Cluster structure

We attempt here to combine all data discussed above in a single coherent picture of the structure of central Carina. We first test the meaningfulness of the derived extinction values A_V, by comparing them with the spectroscopic gravity index γ defined in Damiani et al. (2014). The prediction that we test here is that all main-sequence stars later than mid-G, and only observable in the foreground of the nebula, must have $A_V \leq A_V^{\rm fg}$, while most giants appear in the background with a much lower space density but higher luminosity. Figure 16 shows that this is exactly the case: high-gravity, main-sequence GKM stars have $\gamma < 0.97$ and the vast majority of them are found at $A_V \leq A_V^{\rm fg}$, while giants (having $\gamma > 1.02$) are almost all found in the A_V range between 2–5 mag, typically larger than the extinction toward cluster members.

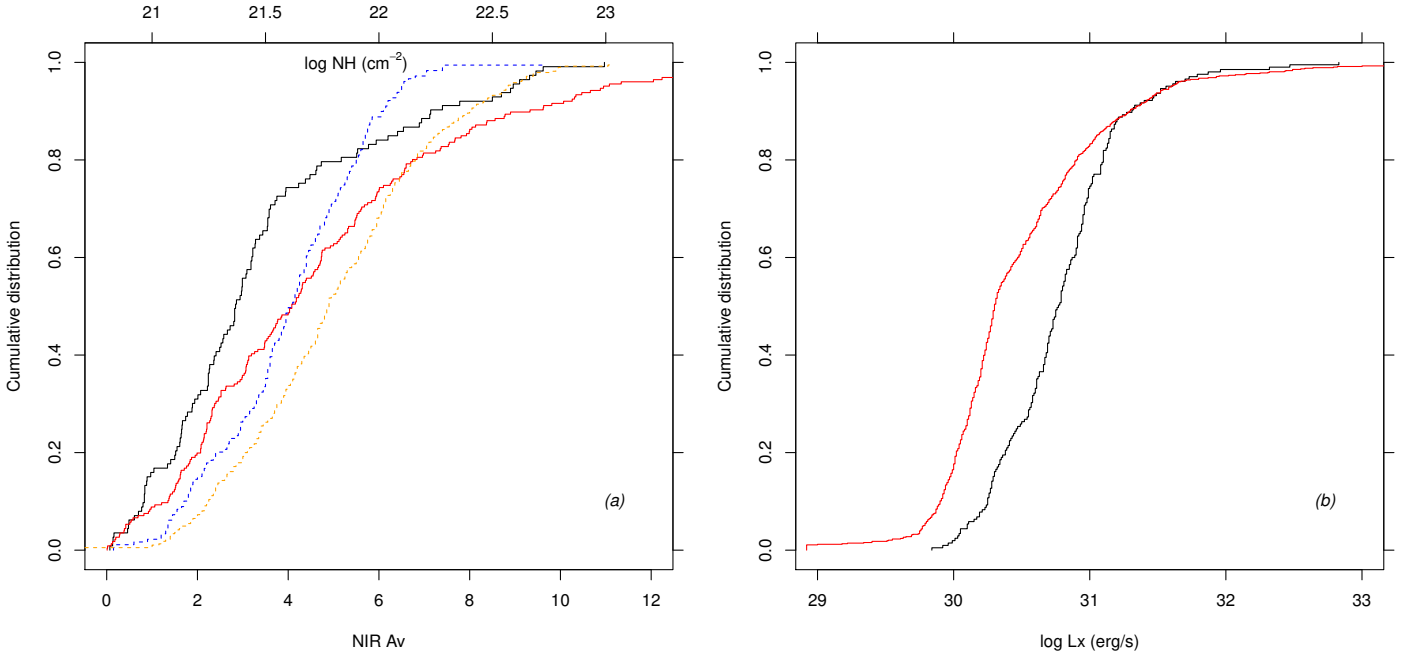

Fig. 15. **a)** Cumulative distributions of A_V (derived from NIR colors) for Tr 16 X-ray sources observed here spectroscopically (black solid line) and unobserved (red solid line). Blue and orange dashed lines indicate the cumulative distributions of gas column density N_H (scale on top axis) for the same subsamples, respectively; **b)** as in panel **a)**, for the X-ray luminosity L_X.

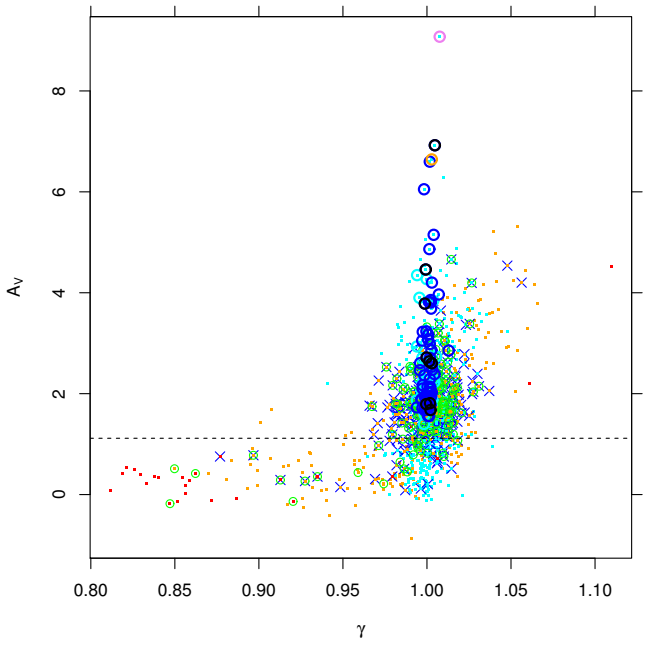

Fig. 16. Optical extinction A_V vs. spectral index γ. Symbols as in Figs. 5 and 10. For GKM stars, γ is an effective gravity diagnostic, where high-gravity stars have $\gamma < 0.97$ and giants have $\gamma > 1.02$. The horizontal dashed line indicates the foreground extinction value.

Having better established our confidence in the determined extinction values, we next consider the spatial distributions of stars in several ranges of A_V, as shown in Fig. 17. The upper left panel shows all stars with $A_V < 0.8$; no clustering is detectable, in agreement with these being foreground stars, unrelated to Carina and its obscuring material. Tens of stars are found projected against the dark V-shaped dust lanes. The number of low-gravity stars (red circles) is very low. In the upper right panel, the low-extinction cluster members appear in dense groups with close spatial association with the most massive stars; the dust lanes are almost devoid of stars except for a dozen (probably background) stars near WR25, where the total absorption is lower than elsewhere in the lane (see, e.g., Fig. 1 in Albacete-Colombo et al. 2008). Most of the B-type stars have not yet made their appearance in this A_V range. This probably makes the number ratio between early-type and solar-type stars more representative of its real value. In the next extinction range, shown in the lower left panel, the stellar distribution has changed considerably. Low-mass members are more widely dispersed away from the most massive stars, while their density generally increases toward places of higher obscuration. This is seen in the vicinity of η Car, which now has many more neighbors toward SE (where they eventually meet the dark lane) than toward NW, and also in the Trumpler 14 region, where again member stars are found exclusively on the side of the cluster nearest the dark lane. Taking the dashed black lines in the figure as a reference, we may observe that the number of stars in their immediate vicinity, in both the Tr 14 and η Car subregions, increases dramatically from the low-extinction layer to the higher extinction layer. This is also true for the B and early-A stars, most of which are found on the high-extinction sides of Tr 14 and η Car, respectively. The southwest and northeast regions around WR25 and HD 93250-Collinder 232, respectively, show several low-gravity background giants, indicating that the total nebula extinction in those regions does not exceed $A_V \sim 2-3$. No background giants are instead found on the high-extinction sides of Tr 14 and η Car, nor in the dark lanes (except for the vicinity of WR25 as already remarked). Finally, the lower right panel shows the most reddened stars found in our dataset. Only early-type cluster members are found here, including the two candidate O stars (both under the SE obscuring lane) and three candidate B supergiants; at these extinction values, background giants make their appearance even close to the SE dark lane, but not in the region surrounding Tr 14. This extinction pattern agrees qualitatively with that in Smith & Brook (2007; their Fig. 5a).

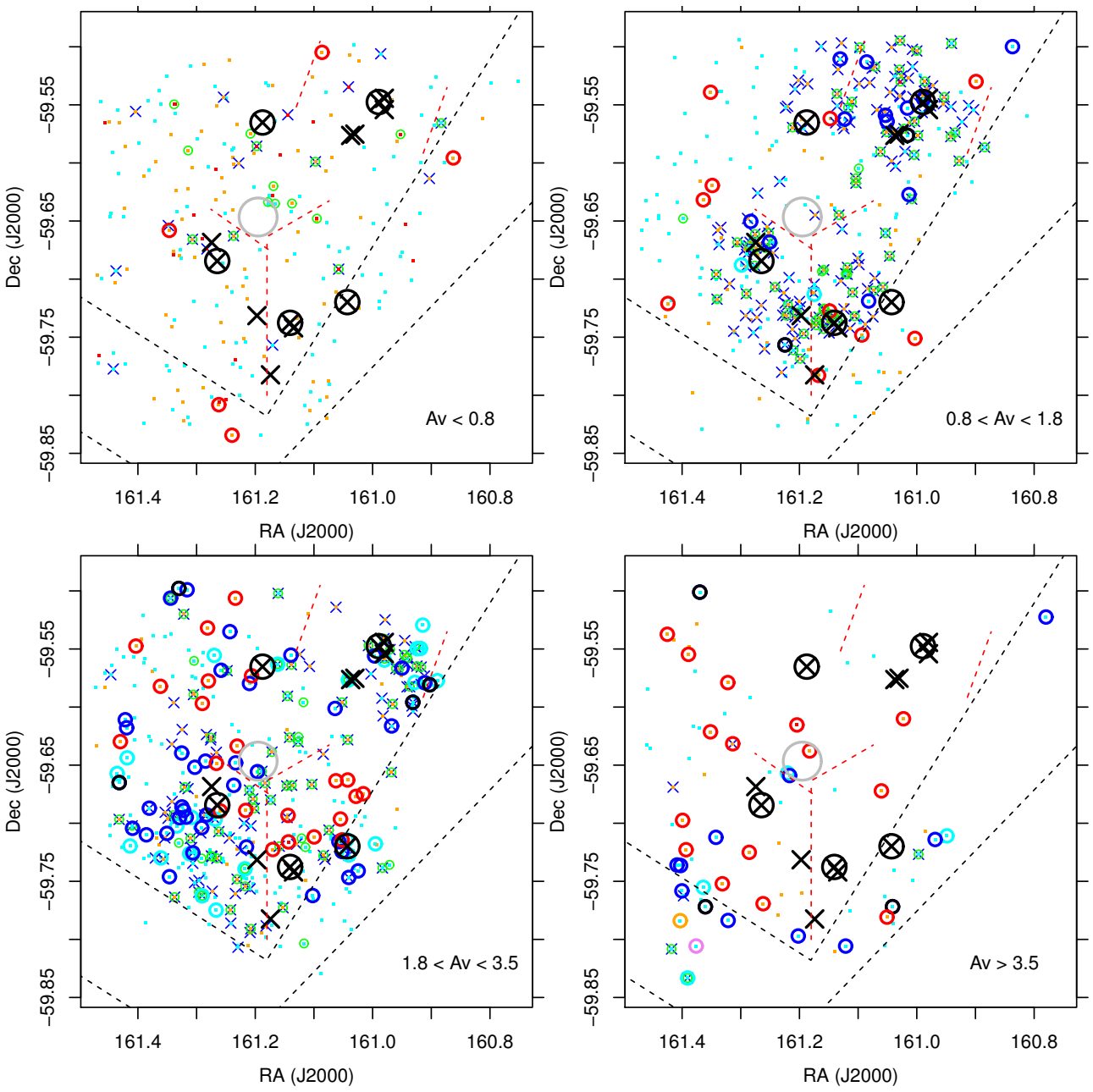

Fig. 17. Spatial maps of observed stars, split in four ranges of A_V as labeled. Star symbols as in Fig. 10 with the addition of red circles indicating low-gravity giants as in Fig. 12. Dashed black lines indicate the dark dust lanes as in Fig. 10. Dashed red segments indicate the boundaries of large gas shells studied in Paper I. The big gray circle indicates the position and approximate size of the Keyhole nebula.

Figure 18 shows all stars with $A_V > 1.8$ together with X-ray detected sources in Tr 16 (most of which are members as discussed above) with X-ray hardness index $HS > 0.5$ [9], which indicates moderate to high absorption; in addition, these X-ray sources were not observed spectroscopically. Most moderately obscured X-ray sources (orange triangles) lie south of η Car and between it and WR25, while the heavily obscured X-ray sources (brown triangles) lie behind the sourthern dark lane with the largest source density found between the two new candidate O stars. This subcluster of highly absorbed X-ray sources is named CCCP-Cl 14 in Feigelson et al. (2011) and Tr 16 SE in Sanchawala et al. (2007). The dominant star of this subcluster, according to Feigelson et al. (2011), is the O eclipsing binary FO 15 (=V662 Car, O5.5Vz + O9.5 V, v), which however we did not observe spectroscopically. The optical extinction of this star is $A_V \sim 5$ (Niemela et al. 2006), thus lower than that we find for our candidate O stars [S87b] IRS 42 and IRS 38 ($A_V = 6.6$ and 9.1, respectively) in the same region. At the same location, an obscured cluster of massive stars was found from *Spitzer* images by Smith et al. (2010; called "cluster G" in their Table 4), who argued that this is not an embedded, extremely young cluster, but more likely a cluster of age 1–2 Myr behind and not inside the foreground dark lane.

Figure 18 shows no clear separation between subclusters in proceeding from η Car to its SE, but only a gradually increasing proportion of highly absorbed Carina members, both massive and of low mass (the latter only from X-rays). Instead, the

[9] *HS* is defined as the count ratio between bands [2–8] keV and [0.5–2] keV.

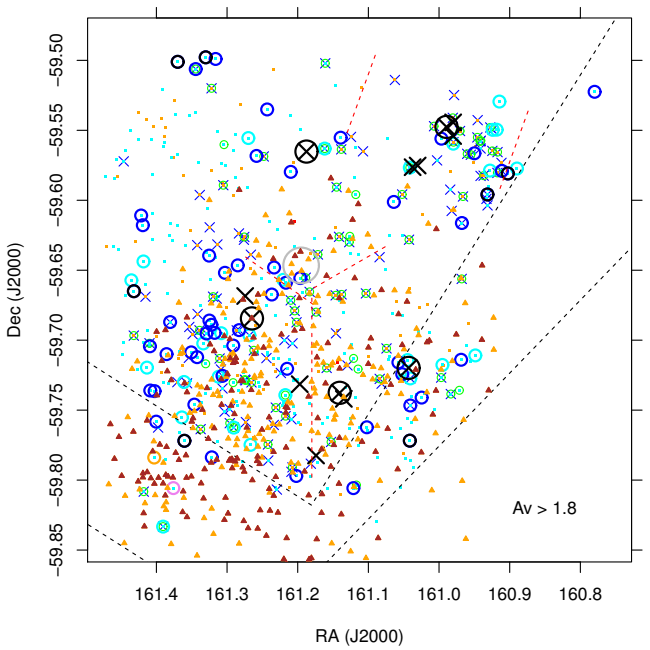

Fig. 18. Spatial map of reddened sample stars with $A_V > 1.8$ (shown by same symbols as in Fig. 17) and of obscured X-ray sources (orange triangles: $0.5 < HS < 1.0$; brown triangles: $HS > 1$).

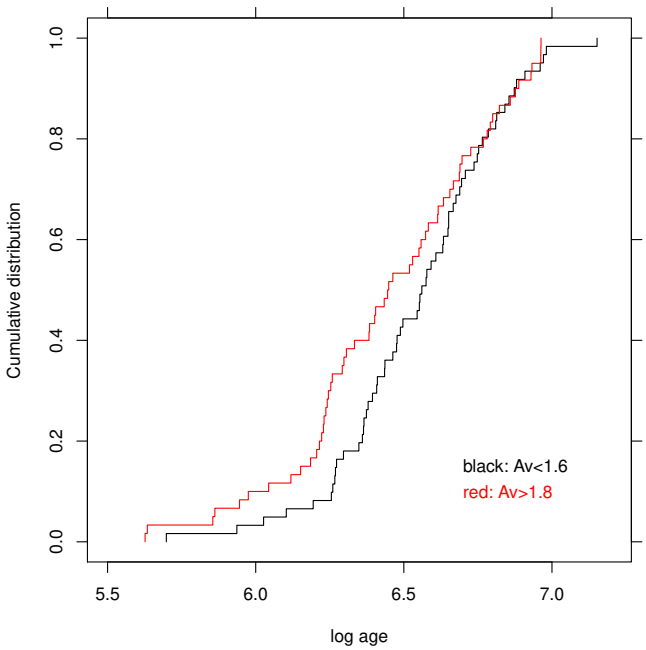

Fig. 19. Cumulative distributions of photometric ages for all members in the $T_{\rm eff}$ range 4300–6500 K. The black line represents stars with $A_V < 1.6$; the red line represents stars with $A_V > 1.8$.

low-extinction members (in Fig. 17, upper right panel) are much more clustered in tight groups centered on the respective massive stars. It is interesting to compare the distribution of stars with that of the ionized gas from Paper I, consisting of several large shells, almost devoid of dust, centered on η Car, WR25, and Tr 14. The observed gradual increase in extinction toward the SE, if most stars are enclosed in such dust-free shells, implies that the obscuring material must lie in front of the star clusters (and gas) and is not generally mixed with them. At its SE border, the η Car gas shell does not seem to interact with matter in the dark lane, but instead fades behind it. This agrees with the conclusion by Smith et al. (2010) that the obscured SE subcluster (their "cluster G") lies behind the lane and does not interact with it. This is probably also true of the newly found massive OB stars in the direction of the dark lanes, so that their UV radiation would illuminate most cluster stars with little attenuation, despite the very large extinction found toward us. Of course, circumstellar dust may still exist around individual stars, which contributes to the A_V scatter in Fig. 17 and shields the massive star UV flux; however, since we do observe a regular spatial extinction pattern in Fig. 17, local extinction is probably a minor contributor to the total observed A_V.

Behind the high-reddening members of Tr 14, with $A_V \leq 3$, we do not find virtually any background star. Except for the Tr 14 region and the dark lanes, we have instead found background giants throughout most of the surveyed part of Carina and, therefore, we have been observing the brightest members through the entire thickness of the nebula to its far side.

10. Stellar ages

We investigate whether there are measurable age differences between the Carina subclusters. A useful age diagnostic for young low-mass stars is the lithium resonance line at 6707 Å, whose EW as a function of $T_{\rm eff}$ was shown in Fig. 5. In the temperature range of the Carina members studied here, however, lithium EW is insensitive to age if a cluster is younger than several tens Myr (Jeffries 2014), as is the case for Carina clusters. Accordingly, the scatter of data points in the above figure may be entirely accounted for by errors on $T_{\rm eff}$ (~5%) and lithium EW and is not related to real age differences among the observed Carina members.

We examine the relative ages of the different Carina subgroups as derived from the star location in the CMD, compared to Siess et al. (2000) isochrones. This methods still benefits from our spectroscopic data since apparent star colors and magnitudes are individually dereddened using the extinction values A_V derived above. In addition, there remain a series of caveats related to nonphotospheric contributions, such as veiling in accreting PMS members, uncertainties in the reddening law, or unrecognized binaries.

The distributions of photometric ages for low- and high-extinction subsamples are shown in Fig. 19; both distributions are rather wide, over more than one dex in age. This agrees with the earlier result of DeGioia-Eastwood et al. (2001) that star formation in these clusters was active over the last 10 Myr, which should be taken as an upper limit to the true age spread considering, for example uncertainties in extinction and reddening law, binarity, or variability. The difference between the two distributions in the figure points to the obscured Carina population being slightly younger than the unobscured one, however with a modest statistical significance of 93.9%.

To corroborate this result, we show in Fig. 20 the cumulative distributions of A_V for Carina members with and without a YSO counterpart in the Zeidler et al. (2016) catalog: (younger) members associated with a YSO have a larger extinction than (older) members with no YSO association, with a confidence level of 99.6%.

The cumulative distributions of photometric ages of Carina member stars in the subclusters are shown in Fig. 21. Stars in Tr 14 are significantly younger (at 99.1% level) than those of all other subgroups (cumulatively), while the age distributions of η Car, HD 93250, and WR25 subgroups are indistinguishable

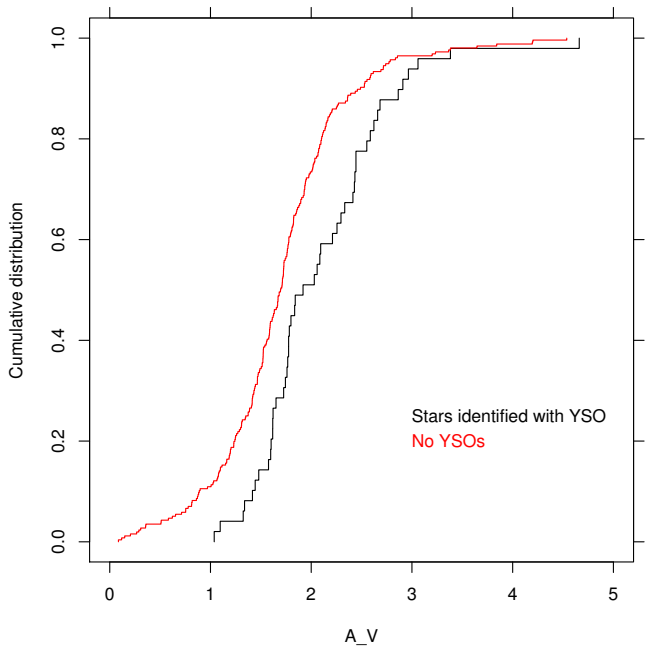

Fig. 20. Cumulative A_V distribution for members identified with a YSO from Zeidler et al. (2016, black line) and for those without a YSO counterpart (red).

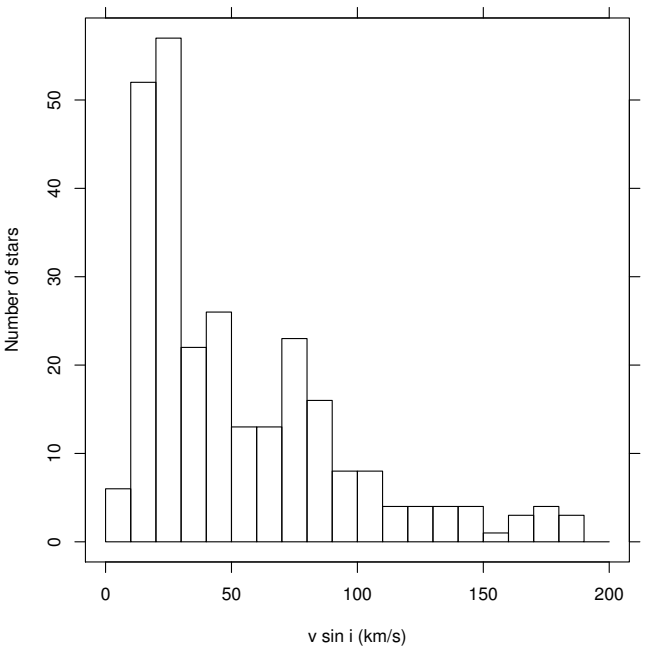

Fig. 22. $v \sin i$ distribution for Carina members with $4500 < T_{\rm eff} < 6500$ K.

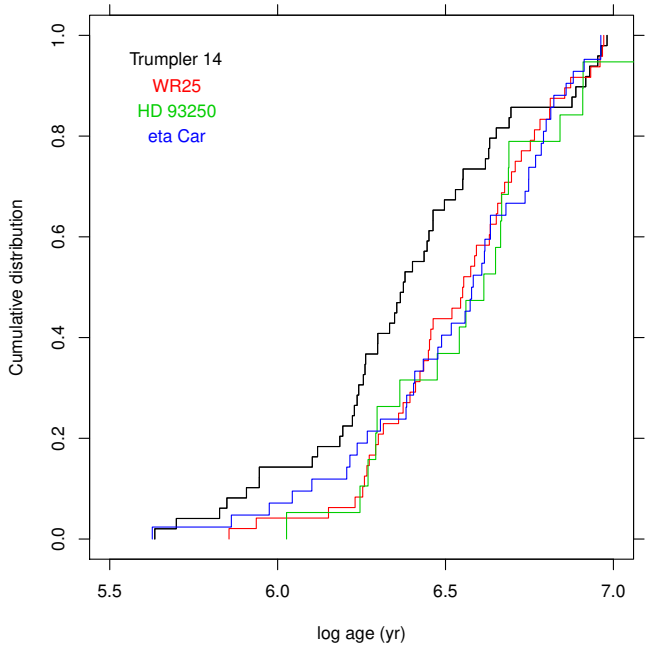

Fig. 21. Cumulative distributions of stellar ages as derived from photometry and isochrones, as in Fig. 13, for cluster members from different subgroups.

from one another. This agrees with the already mentioned suggestion that Tr 14 is younger than Tr 16.

11. Rotation

The HR15n spectra of Carina members show that a large percentage of these stars, including lower mass ones, are fast rotators, with a median $v \sin i \sim 40$ km s^{-1} for $4500 < T_{\rm eff} < 6500$ K (Fig. 22). To our knowledge, these are the first measurements of rotation rates for Carina PMS stars. Since average stellar rotation rates are strongly mass dependent, we have chosen a restricted $T_{\rm eff}$ range for the above figure. Moreover, the figure suggests a bimodal distribution with a higher peak near $v \sin i \sim 22$ km s^{-1}, and a secondary one at $v \sin i \sim 75$ km s^{-1}, qualitatively similar to that in the ONC (Stassun et al. 1999, Herbst et al. 2002) for masses larger than 0.25 $M_\odot$. Assuming a typical radius for our Carina PMS stars of 2 $R_\odot$, the $v \sin i$ peaks would transform into rotational-period peaks around 1.1 and 3.6 days, respectively, which is not significantly different from those found in the ONC. We do not find a significant difference between the rotational velocity distributions of CTTS and WTTS either globally or considering each subgroup separately; however, as we discussed in Sect. 3, an accurate assessment of CTTS status is difficult using our spectra. We therefore examined the $v \sin i$ distributions for stars with and without NIR excesses, as measured using the 2MASS $(H-K, J-H)$ color–color diagram (as, e.g., in Damiani et al. 2006b) or the *Spitzer* IRAC ([3.6−4.5], [5.8−8.0]) diagram (as in Povich et al. 2011b). In our Carina sample only very few stars are found with significant excesses in these NIR or MIR colors, and their rotational-velocity distribution is not significantly different from that of stars with no excesses. Last we have considered our Carina members with a counterpart in the YSO catalog of Zeidler et al. (2016): the $v \sin i$ distributions for stars associated and unassociated with a YSO are different at the 92.5% significance level. This is marginal, probably because of the limited member sample size. The sense of the difference, nevertheless, seems to indicate that stars surrounded by a massive dust disk spin slower than stars with no disk, which offers some support to the disk-locking paradigm (e.g., Mathieu 2004; Rebull et al. 2006).

We find a more significant difference (at 98.55% level) between sample stars younger and older than 3 Myr (Fig. 23), respectively. The older stars rotate more slowly than younger ones. This result is similar to that found by Littlefair et al. (2011) for several other young clusters. This is surprising for mostly diskless PMS stars, which should spin up as their moment of inertia decreases during contraction. However, stars in this Carina PMS sample belong mostly to the mass range 1−4 $M_\odot$, and

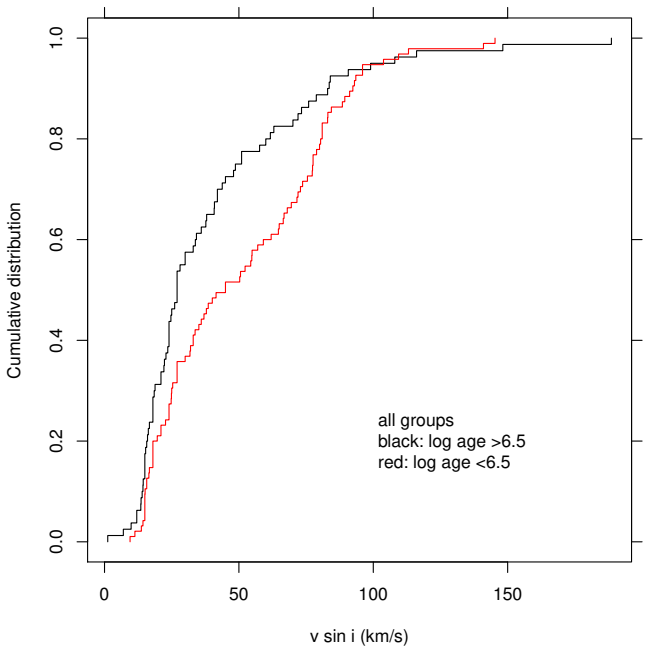

Fig. 23. Cumulative $v \sin i$ distributions for low-mass member stars from all groups, split by photometric age. The black line indicates log age >6.5; the red line indicates log age <6.5 (yr).

nearly half of them lie along radiative tracks, where contraction is much slower than along the Hayashi track; according to the Siess et al. (2000) models, the radius even increases along part of the radiative track for some masses in this range. The richness of Carina, coupled with our limiting magnitude, renders the stellar mass composition of our sample very much complementary to that of most existing studies of rotation in young clusters. We are unable to study the rotation of stars below ~1 $M_{\odot}$, but have a sample of PMS stars in the ~1−4 $M_{\odot}$ range of a size hardly found in any other studied cluster. Therefore, the Carina rotation data can be very important to study the rotational evolution of PMS stars along their radiative track. Similar datasets are still lacking for SFRs in the same richness class as Carina, like those mentioned in Sect. 1.

Besides the difference between younger and older Carina members, Fig. 23 shows that the bimodal $v \sin i$ distribution is only found in the younger subsample. The older subsample does not show two bumps in the cumulative distribution; the histogram peaks correspond to the steepest derivatives in the cumulative distribution. This may be related to the development of the radiative stellar core, which has a profound influence on the observed surface rotation (see, e.g., Spada et al. 2011). Again, the Carina rotation data may be crucial for testing theoretical models of rotational evolution along the radiative track.

12. Discussion and conclusions

Our study of the *Gaia*-ESO dataset on Tr 14-16, the richest clusters in the Carina complex, is to our knowledge the first extensive spectroscopic exploration of a sizable sample of stars in a giant SFR, with a mass in excess of 10^4 $M_{\odot}$, of which Carina is a rare example. Out of 1085 stars observed, more than 100 turned out to be early-type stars, mostly lacking a spectroscopic classification; among these stars are two new candidate O stars at high extinction, already known as bright IR sources, 17 candidate Herbig Ae/Be stars, and 9 candidate B supergiants, although the limited wavelength range of the studied data prevented a more detailed classification. Based on RV, lithium, and X-ray data, we find 286 Carina low-mass members. Their number ratio with respect to the massive stars is not representative because the wide range in extinction encountered favors observation of bright member stars at high reddening.

We have confirmed the anomalous reddening law already reported and placed new constraints on the three-dimensional space distributions of Carina members. In central Carina, there is a relatively small percentage of embedded YSOs (Povich et al. 2011); this and other constraints posed by our previous study of the ionized gas distribution (Paper I) suggest a picture where the extinction toward Carina young stars in the η Car-Tr 16 region is mostly caused by dust at some distance from the stars themselves that is not mixed with them. This has impact on the amount of UV flux they receive from the most massive cluster stars and on the consequences that this is likely to have on the evolution of the circumstellar disks (photoevaporation). It is worth noting that some information on the local level of UV irradiation may also come from a detailed analysis of some of the DIBs found in the red spectra of these stars (Kos & Zwitter 2013).

The geometry of the studied region in Carina is not simple. We observed background giants through several sightlines across the studied region, behind a few magnitudes of optical extinction. The dust lane to SE, close to η Car, produces enough obscuration to drive a candidate O star close to our limiting magnitude; of course, still more deeply obscured massive stars may exist in the same direction. If a blister geometry applies to this part of the cloud, this must be seen sideways from our sightline. In the Tr 14 region close to the western dark lane, instead, the foreground obscuration is a little more uniform, but rises more sharply toward the dust lane. The two dust lanes have therefore a different placement in space with respect to their nearest cluster.

The data suggest a complex history of star formation, with a significantly younger age for Trumpler 14 with respect to all other Carina subgroups. The high-extinction stars are only slightly younger than the low-extinction ones, and more frequently associated with a YSO.

Because of its richness, Carina also provides us with a sample of PMS stars in the 1−4 $M_{\odot}$ range of a size hardly found in other young clusters. We have presented $v \sin i$ distributions for this unique sample of stars; our sample is significantly larger than, for example, the sample found in the study of intermediate-mass star rotation by Wolff et al. (2004), in the ONC. About one-half of these stars are evolving along radiative tracks. We find evidence of a bimodal $v \sin i$ distribution, analogous to that found in the ONC for lower mass stars. Stars older than 3 Myr, and mostly on their radiative PMS track, are found to rotate more slowly than younger stars, which puts constraints on the rotational evolution of intermediate-mass PMS stars.

Acknowledgements. We wish to thank an anonymous referee for his/her helpful suggestions. Based on data products from observations made with ESO Telescopes at the La Silla Paranal Observatory under program ID 188.B-3002. These data products have been processed by the Cambridge Astronomy Survey Unit (CASU) at the Institute of Astronomy, University of Cambridge, and by the FLAMES/UVES reduction team at INAF/Osservatorio Astrofisico di Arcetri. These data have been obtained from the *Gaia*-ESO Survey Data Archive, prepared and hosted by the Wide Field Astronomy Unit, Institute for Astronomy, University of Edinburgh, which is funded by the UK Science and Technology Facilities Council. This work was partly supported by the European Union FP7 program through ERC grant number 320360 and by the Leverhulme Trust through grant RPG-2012-541. We acknowledge the support from INAF and Ministero dell'Istruzione, dell'Università' e della Ricerca (MIUR) in the form of the grant "Premiale VLT 2012". The results presented here benefit from discussions held during the *Gaia*-ESO workshops and conferences supported by the ESF (European Science Foundation) through the GREAT Research Network

Programme. R.B. acknowledges financial support from INAF under PRIN2013 Programme "Disks, jets and the dawn of planets". This research has made use of the SIMBAD database, operated at CDS, Strasbourg, France. This work was also using data products from observations made with ESO Telescopes at the La Silla Paranal Observatory under program ID 177.D-3023, as part of the VST Photometric Hα Survey of the Southern Galactic Plane and Bulge (VPHAS+, www.vphas.eu).

References

Albacete-Colombo, J. F., Damiani, F., Micela, G., Sciortino, S., & Harnden, F. R., Jr. 2008, A&A, 490, 1055
Antokhin, I. I., Rauw, G., Vreux, J.-M., van der Hucht, K. A., & Brown, J. C. 2008, A&A, 477, 593
Bagnulo, S., Jehin, E., Ledoux, C., et al. 2003, The Messenger, 114, 10
Barbá, R. H., Gamen, R. C., Arias, J. I., et al. 2010, Rev. Mex. Astron. Astrofís., 38, 30
Bessell, M. S., Castelli, F., & Plez, B. 1998, A&A, 333, 231
Broos, P. S., Townsley, L. K., Feigelson, E. D., et al. 2011a, ApJS, 194, 2
Broos, P. S., Getman, K. V., Povich, M. S., et al. 2011b, ApJS, 194, 4
Carraro, G., Romaniello, M., Ventura, P., & Patat, F. 2004, A&A, 418, 525
Damiani, F., Micela, G., Sciortino, S., et al. 2006a, A&A, 460, 133
Damiani, F., Prisinzano, L., Micela, G., & Sciortino, S. 2006b, A&A, 459, 477
Damiani, F., Prisinzano, L., Micela, G., et al. 2014, A&A, 566, A50
Damiani, F., Bonito, R., Magrini, L., et al. 2016, A&A 591, A74
DeGioia-Eastwood, K., Throop, H., Walker, G., & Cudworth, K. M. 2001, ApJ, 549, 578
Drew, J. E., Gonzalez-Solares, E., Greimel, R., et al. 2014, MNRAS, 440, 2036
Ekström, S., Georgy, C., Eggenberger, P., et al. 2012, A&A, 537, A146
Feigelson, E. D., Getman, K. V., Townsley, L. K., et al. 2011, ApJS, 194, 9
Flaccomio, E., Damiani, F., Micela, G., et al. 2003, ApJ, 582, 398
Frasca, A., Biazzo, K., Lanzafame, A. C., et al. 2015, A&A, 575, A4
Gilmore, G., Randich, S., Asplund, M., et al. 2012, The Messenger, 147, 25
Grigsby, J. A., Morrison, N. D., & Anderson, L. S. 1992, ApJS, 78, 205
Herbst, W., Bailer-Jones, C. A. L., Mundt, R., Meisenheimer, K., & Wackermann, R. 2002, A&A, 396, 513
Hur, H., Sung, H., & Bessell, M. S. 2012, AJ, 143, 41
Jeffries, R. D. 2014, EAS Pub. Ser., 65, 289
Kalari, V. M., Vink, J. S., Drew, J. E., et al. 2015, MNRAS, 453, 1026
Kenyon, S. J., & Hartmann, L. 1995, ApJS, 101, 117
Kos, J., & Zwitter, T. 2013, ApJ, 774, 72
Lada, C. J., & Lada, E. A. 2003, ARA&A, 41, 57
Lanz, T., & Hubeny, I. 2003, ApJS, 146, 417
Lanzafame, A. C., Frasca, A., Damiani, F., et al. 2015, A&A, 576, A80
Littlefair, S. P., Naylor, T., Mayne, N. J., Saunders, E., & Jeffries, R. D. 2011, MNRAS, 413, L56
Maíz Apellániz, J. 2004, PASP, 116, 859
Maíz Apellániz, J. 2005, PASP, 117, 615
Maíz Apellániz, J. 2006, AJ, 131, 1184
Maíz Apellániz, J. 2007, in The Future of Photometric, Spectrophotometric and Polarimetric Standardization, ed. C. Sterken, ASP Conf. Ser., 364, 227
Maíz Apellániz, J. 2013a, in Highlights of Spanish Astrophysics VII, 657
Maíz Apellániz, J. 2013b, in Highlights of Spanish Astrophysics VII, 583
Maíz Apellániz, J. 2015, Mem. Soc. Astron. Ital., 86, 553
Maíz Apellániz, J., & Sota, A. 2008, in Rev. Mex. Astron. Astrofís (Conf. Ser.), 33, 44
Maíz Apellániz, J., Walborn, N. R., Galué, H. Á., & Wei, L. H. 2004, ApJS, 151, 103
Maíz Apellániz, J., Sota, A., Walborn, N. R., et al. 2011, in Highlights of Spanish Astrophysics VI, eds. M. R. Zapatero Osorio, J. Gorgas, J. Maíz Apellániz, J. R. Pardo, & A. Gil de Paz, 467
Maíz Apellániz, J., Evans, C. J., Barbá, R. H., et al. 2014, A&A, 564, A63
Maíz Apellániz, J., Negueruela, I., Barbá, R. H., et al. 2015, A&A, 579, A108
Mathieu, R. D. 1994, ARA&A, 32, 465
Mathieu, R. D. 2004, Stellar Rotation, 215, 113
Mayne, N. J., Naylor, T., Littlefair, S. P., Saunders, E. S., & Jeffries, R. D. 2007, MNRAS, 375, 1220
McErlean, N. D., Lennon, D. J., & Dufton, P. L. 1999, A&A, 349, 553
Negueruela, I., Maíz-Apellániz, J., Simón-Díaz, S., et al. 2015, in Highlights of Spanish Astrophysics VIII, 524
Niemela, V. S., Morrell, N. I., Fernández Lajús, E., et al. 2006, MNRAS, 367, 1450
Povich, M. S., Townsley, L. K., Broos, P. S., et al. 2011a, ApJS, 194, 6
Povich, M. S., Townsley, L. K., Broos, P. S., et al. 2011b, ApJS, 194, 14
Preibisch, T., Kim, Y.-C., Favata, F., et al. 2005, ApJS, 160, 401
Randich, S., Gilmore, G., & Gaia-ESO Consortium 2013, The Messenger, 154, 47
Rebolledo, D., Burton, M., Green, A., et al. 2016, MNRAS, 456, 2406
Rebull, L. M., Stauffer, J. R., Megeath, S. T., Hora, J. L., & Hartmann, L. 2006, ApJ, 646, 297
Sanchawala, K., Chen, W.-P., Lee, H.-T., et al. 2007, ApJ, 656, 462
Schmitt, J. H. M. M. 1997, A&A, 318, 215
Siess, L., Dufour, E., & Forestini, M. 2000, A&A, 358, 593
Sigut, T. A. A. 1996, ApJ, 473, 452
Simón-Díaz, S., Castro, N., García, M., & Herrero, A. 2011, in IAUS, 272, 310
Smith, R. G. 1987, MNRAS, 227, 943
Smith, N. 2006, ApJ, 644, 1151
Smith, N., & Brooks, K. J. 2007, MNRAS, 379, 1279
Smith, N., & Brooks, K. J. 2008, in Handbook of Star Forming Regions, Vol. II, 138
Smith, N., Povich, M. S., Whitney, B. A., et al. 2010, MNRAS, 406, 952
Sota, A., Maíz Apellániz, J., Morrell, N. I., et al. 2014, ApJS, 211, 10
Spada, F., Lanzafame, A. C., Lanza, A. F., Messina, S., & Collier Cameron, A. 2011, MNRAS, 416, 447
Stassun, K. G., Mathieu, R. D., Mazeh, T., & Vrba, F. J. 1999, AJ, 117, 2941
Tapia, M., Roth, M., Vázquez, R. A., & Feinstein, A. 2003, MNRAS, 339, 44
Townsley, L. K., Broos, P. S., Corcoran, M. F., et al. 2011, ApJS, 194, 1
Vaidya, K., Chen, W.-P., & Lee, H.-T. 2015, AJ, 150, 195
Walborn, N. R. 1973, ApJ, 179, 517
Walborn, N. R. 1995, Rev. Mex. Astron. Astrofis. Conf. Ser., 2, 51
Wolff, S. C., Strom, S. E., & Hillenbrand, L. A. 2004, ApJ, 601, 979
Wolk, S. J., Broos, P. S., Getman, K. V., et al. 2011, ApJS, 194, 12
Zeidler, P., Preibisch, T., Ratzka, T., Roccatagliata, V., & Petr-Gotzens, M. G. 2016, A&A, 585, A49

Appendix A: Sky-subtraction procedure

The *Gaia*-ESO HR15n dataset on Tr 14-16 contains 185 pure-sky spectra from 137 distinct sky positions, taken simultaneously with the stellar spectra. We have identified the following components in these sky spectra:

1. Sky-glow emission lines from Earth atmosphere: nearly identical within spectra from the same Observing Block, variable with time (from an Observing Block to the next), narrow within instrumental resolution, at fixed wavelength in Earth frame.
2. Scattered solar light (typically moonlight): continuum with absorption lines, being essentially a solar spectrum at very low levels. Constant within the same Observing Block, but changing from one Observing Block to the next.
3. Nebular Hα, He I, [N II], and [S II] lines: they originate from physically large regions near the target stars and do not vary with time, but have a strong spatial dependence in their strengths, line shapes, widths, and velocities (see Paper I).
4. Nebular continuum emission, from reflection nebulosity: a non-negligible component in Tr 14-16, free of solar-like spectral features but with a rather flat spectrum (like massive stars in the nebula), time constant but space variable (Paper I).

The standard *Gaia*-ESO pipeline is able to remove components 1–2 (constant within the same Observing Block, variable in time), but is not able to deal with components 3–4. Conversely, an attempt to correct a star spectrum using only the sky spectrum nearest on the sky would have more success in dealing with components 3–4, but would perform badly on components 1–2, when these are significant. Clearly, in the complex case of Tr 14-16 a combined approach is needed.

Stellar parameter evaluation relies on the depth of stellar absorption lines or bands, so that an accurately determined stellar continuum is of the greatest importance. Contamination by sky glow or nebular lines is in this context a minor problem, affecting very localized wavelength regions or lines, which may be usually ignored in deriving star parameters (except for the case of Hα). We therefore focus first on sky continuum determination and correction.

In the Tr 14-16 dataset we find, using two methods, that the sky continuum does not contain traces of scattered sunlight. We computed the cross-correlation function (CCF) of the sky spectra (nebular lines excluded) with a solar spectrum, looking for any peak near RV = 0, but no such peak was found for any Observing Block. A second method was to fit the sky spectrum with a constant, flat spectrum plus a scaled solar spectrum: again, the scaling factor for the solar spectrum was negligibly small with respect to the other, flat, component, for all Observing Blocks. Instead, within the same Observing Block the median sky continuum level is found to vary significantly, and with a clear spatial pattern, which is a clear indication of a nebular (reflection) origin for this sky spectrum component.

In Tr 14-16, the absence of scattered solar continuum enables us to eliminate all time-variable sky signatures by just subtracting out the sky-glow lines. This leaves a purely "star plus nebular" spectrum, and the nebular part is later estimated from the whole set of (nonsimultaneous) sky spectra in the same dataset. Sky-glow lines in the HR15n range, of sufficient intensity as to merit consideration in this context, are no more than 20 narrow lines. In principle, also some geocoronal Hα emission is expected, but in practice it is not detected against the enormously brighter Hα emission from the nebula. For each Observing Block, the sky-glow line spectrum, net of the adjacent continuum intensity and averaged within the same Observing Block, was computed and subtracted out from all spectra in the same Observing Block to obtain "star plus nebular" or "nebular-only" spectra for stellar and sky spectra, respectively.

Having eliminated terrestrial sky features in this way, the problem now reduces to estimate the most appropriate nebular spectrum to be used for correcting a given stellar spectrum. Since the spatial density of sky fibers (considering all Observing Blocks together) is much less than that of target star fibers, the correspondence between the nebular (and sky-continuum) emission in a stellar spectrum and in its nearest-neighbor sky spectrum is never found to be perfect. Distances between a given star and its nearest sky fiber are of order of 30″ or more: the nebular morphology is here so complex that there is no guarantee that even the nearest sky is a good approximation to the sought nebular spectrum at the star position; one gets an idea of the range of variation of nebular spectrum in the vicinity of a given star by looking at more (say five) sky positions nearby. Therefore, we subtracted the nebular spectra from stellar spectra five times per star using its nearest five sky positions. Since the properties of nebular emission sometimes vary sharply and definitely nonlinearly in space, this is considered a robust method (within the limitations of the available data) to understand the uncertainties involved in the procedure.